Setting of the Poincaré section for accurately calculating the phase of rhythmic spatiotemporal dynamics

Takahiro Arai , ^{1,*} Yoji Kawamura , ¹ and Toshio Aoyagi ²

¹Center for Mathematical Science and Advanced Technology, Japan Agency for Marine-Earth Science and Technology, Yokohama 236-0001, Japan

²Graduate School of Informatics, Kyoto University, Yoshida-Honmachi, Sakyo-ku, Kyoto 606-8501, Japan



(Received 24 July 2024; accepted 10 December 2024; published 6 January 2025)

Synchronization analysis of real-world systems is essential across numerous fields, including physics, chemistry, and life sciences. Generally, the governing equations of these systems are unknown, and thus, the phase is calculated from measurements. Although existing phase calculation techniques are designed for oscillators that possess no spatial structure, methods for handling spatiotemporal dynamics remain undeveloped. The presence of spatial structure complicates the determination of which measurements should be used for accurate phase calculation. To address this, we explore a method for calculating the phase from measurements taken at a single spatial grid point. The phase is calculated to increase linearly between event times when the measurement time series intersects the Poincaré section. The difference between the calculated phase and the isochron-based phase, resulting from the discrepancy between the isochron and the Poincaré section, is evaluated using a linear approximation near the limit-cycle solution. We found that the difference is small when measurements are taken from regions that dominate the rhythms of the entire spatiotemporal dynamics. Furthermore, we investigate an alternative method where the Poincaré section is applied to time series obtained through orthogonal decomposition of the entire spatiotemporal dynamics. We present two decomposition schemes that utilize principal component analysis. For illustration, the phase is calculated from the measurements of spatiotemporal dynamics exhibiting target waves or oscillating spots, simulated by weakly coupled FitzHugh-Nagumo reaction-diffusion models.

DOI: 10.1103/PhysRevE.111.014205

I. INTRODUCTION

Researchers across various disciplines, including physics, chemistry, and life sciences, have shown significant interest in the dynamics of coupled self-sustained oscillators. According to the phase reduction theory [1,2], a multidimensional nonlinear system can be simplified to a phase equation with a single phase variable representing the oscillator state. This equation illustrates how coupling functions influence oscillation rhythms. This theory not only aids in the experimental and theoretical analysis of synchronization properties in weakly coupled nonlinear oscillators [3–7] but also supports an inverse problem framework, enabling causality to be inferred from measurements through a concise description. Assuming that the system consists of coupled oscillators, this framework allows us to characterize the variations in oscillatory rhythms through phase equations.

The inverse problem of identifying the direction of coupling [8], phase sensitivity function [9–14], or phase coupling function [15–24] requires developing methods to calculate the phase time series from measurements. This is because the inverse problem utilizes the phase time series to obtain phase equations incorporating the phase coupling function between the oscillators and the phase sensitivity function, which quantifies linear response characteristics of the phase

*Contact author: araitak@jamstec.go.jp

to weak perturbations. Therefore, accurately calculating the phase is crucial for understanding the properties of systems. A straightforward method for phase calculation involves linearly interpolating the phase over one period, measured using the Poincaré section. Recent studies have developed methods to calculate the phase more accurately [13,14,17,18,25–27]. Furthermore, many studies employ techniques beyond the phase reduction theory including the Hilbert transform [28,29], Koopman operator [30–33], and autoencoder [34,35]. These studies allow the phase to capture fluctuations within a single period caused by continuous perturbations, including noise, coupling functions, and external perturbations. The development of the aforementioned method has provided a valuable tool for uncovering the mechanisms of synchronization in real-world systems [21,36–43].

Many studies have reported that synchronization occurs not only in oscillators but also in spatiotemporal dynamics. For example, in atmospheric and oceanic circulation [44,45], synchronous phenomena are observed between opposite sides of the globe, such as the sea surface temperatures of the Kuroshio Current and the Gulf Stream [46,47], as well as the atmospheric variability patterns of the Arctic Oscillation and the Antarctic Oscillation [48]. This discovery prompted us to create a method for analyzing the synchronization mechanism underlying spatiotemporal dynamics. The phase reduction theory has been broadened beyond its original application to limit-cycle oscillator, now encompassing collective oscillations of dynamical elements [49–52] and

spatiotemporal dynamics, such as the oscillatory convection [53–55], reaction-diffusion system [56,57], periodic flow [58–63], beating flagella [64], and traveling pulses [65–73]. These extended theories offer systematic methods to approximate the rhythmic dynamics of networks with highly multidimensional state space, or spatiotemporal dynamics with infinite-dimensional state space, using one-dimensional and space-independent phase equations. These methods facilitate detailed analysis of synchronization mechanisms both between networks (i.e., internetwork) and between spatiotemporal patterns.

With recent advances in the phase reduction theory, there is growing interest in developing an inverse method to estimate phase equations that characterize spatiotemporal dynamics. However, such an inverse method remains undeveloped because reliable techniques for calculating phase from measurements are lacking. Ideally, phase calculation should remain consistent regardless of which measurements are used, accurately reflecting the rhythm of the overall spatiotemporal dynamics. However, as this study demonstrates, practical phase calculations are dependent on measurements, underscoring the need for theoretical support to achieve accurate phase derivation from empirical data. Furthermore, because of the spatial structure inherent in spatiotemporal dynamics, several considerations arise for phase calculation: (i) determining the optimal locations for fixed-point observations of the dynamics and (ii) exploring the use of modes obtained from spatiotemporal dynamics through decomposition techniques such as principal component analysis (PCA) (see, e.g., Ref. [74]). Calculating the phase of spatiotemporal dynamics from measurements presents a complex challenge, and this issue has not yet been addressed in existing research. This study aims to develop a method that allows for the calculation of phase in spatiotemporal dynamics, analogous to the approach used for limit-cycle oscillators. The method for calculating the phase will be crucial for uncovering causality between spatiotemporal dynamics and providing a clearer, more intuitive understanding of these systems.

In this study, we explore two methods for calculating the phase of the spatiotemporal dynamics: one method relies on measurements taken at a single spatial grid point, while the other method utilizes measurements from all spatial grid points. First, we examine the method for calculating the phase using measurements taken at a single spatial grid point. This method involves a straightforward technique: measuring the period of spatiotemporal dynamics using the Poincaré section applied to the measurement time series, and then linearly interpolating the phase over one period. The accuracy of phase calculation is influenced by the measurement position. Thus, we developed an approach to optimize the measurement position for accurate phase calculation. The difference between the calculated phase and the isochron-based phase can be evaluated using a linear approximation in the vicinity of the limit-cycle solution [56]. To illustrate this approach, we provide an example by calculating the phase of spatiotemporal dynamics simulated by coupled FitzHugh-Nagumo (FHN) reaction-diffusion models. By selecting suitable parameters, the model can generate various spatiotemporal rhythmic patterns [75–78]. In particular, we simulated target waves and oscillating spots. Next, we investigate the method for calculating the phase using measurements from all spatial grid points. In this method, the phase is calculated by linear interpolation, with the Poincaré section applied to a one-dimensional time series obtained from the orthogonal decomposition of the spatiotemporal dynamics. We propose decomposition schemes using PCA and demonstrate how to calculate the phase of spatiotemporal dynamics through numerical simulation with the FHN reaction-diffusion model.

This paper is organized as follows: In Sec. II, we briefly review the phase reduction theory for partial differential equations (PDEs) to introduce the concept of phase [56]. In Sec. III, we present the FHN reaction-diffusion model as a numerical simulation framework. In the following sections, we examine methods for calculating phase time series based on measurements from the numerical simulation. In Sec. IV, we focus on a method using measurements from a single spatial grid point. In Sec. V, we shift focus to a method utilizing measurements across all spatial grid points. Finally, Sec. VI summarizes our findings and discusses future research directions stemming from this study.

Appendices A to G provide detailed supplementary information. Appendices A and B clarify the concept of isochrons defined by phase reduction theory (Sec. II) for ordinary differential equations (ODEs) and PDEs. Appendix C shows the limit-cycle solution and phase sensitivity function for the FHN reaction-diffusion model from Sec. III. Appendix D details the phase equation derived from phase reduction theory. Appendix E covers the phase equation estimation mentioned in Secs. IV and V. Appendix F details the derivation of Eq. (11) in Sec. V.C. Finally, in Appendix G, the phase calculation methods from Secs. IV and V are applied to a different rhythmic spatiotemporal pattern, known as oscillating spots.

II. BRIEF REVIEW OF THE PHASE REDUCTION THEORY FOR A PARTIAL DIFFERENTIAL EQUATION

We consider a pair of weakly coupled reaction-diffusion models. The general form of this dynamical system is described by the following PDE:

$$\frac{\partial}{\partial t} X_1(\mathbf{r}, t) = \mathbf{F}_1(X_1, \mathbf{r}) + D_1 \nabla^2 X_1 + \mathbf{G}(X_1, X_2),
\frac{\partial}{\partial t} X_2(\mathbf{r}, t) = \mathbf{F}_2(X_2, \mathbf{r}) + D_2 \nabla^2 X_2 + \mathbf{G}(X_2, X_1),$$
(1)

where $X_i(\mathbf{r}, t) \in \mathbb{R}^N$ represents the state variable of system i at point r and time t, $F_i(X, r)$ represents the local reaction dynamics at r, $D_i \nabla^2 X_i$ represents the diffusion of X_i over the field with a diffusion matrix D_i , and $G(X_i, X_j) =$ $K[X_i(\mathbf{r},t) - X_i(\mathbf{r},t)]$ represents local and linear mutual couplings with a diagonal matrix K representing the intensity of the mutual coupling. We assume that the reaction-diffusion model, when uncoupled (G = 0), exhibits a limit-cycle solution with a period T_i . Additionally, we consider that the mutual coupling is sufficiently weak, such that the state X_i remains close to the limit-cycle solution. As in an ODE case [1,2], the phase is defined over the basin of attraction of the limit-cycle solution using the concept of isochrons [56] (see Appendix A for the ODE case and Appendix B for the PDE case). We first assign the phase $\phi_i(t) = \omega_i t$ to the state on the limit cycle, ensuring that the phase increases linearly with a

constant frequency $\omega_i := 2\pi/T_i$. The state on the limit-cycle solution corresponding to ϕ_i is represented by $\chi_i(\mathbf{r}, \phi_i)$. This state satisfies $\chi_i(\mathbf{r}, \phi_i) = \chi_i(\mathbf{r}, \phi_i + 2\pi)$ owing to the 2π periodicity. Next, we extend the phase assignment to the entire basin of attraction of the limit-cycle solution, enabling us to assign a phase to the state variable X_i even when it is not on the limit cycle. As a result, the phase ϕ_i approximately represents the state X_i . The fluctuation of the phase reflects the changes in the rhythm of spatiotemporal dynamics due to the mutual coupling G.

III. NUMERICAL SIMULATION WITH A PAIR OF WEAKLY COUPLED FHN REACTION-DIFFUSION MODELS

Our goal is to develop a method for calculating phase time series directly from measurements of spatiotemporal dynamics, enabling identification of the phase without requiring prior knowledge of the governing equations. In this study, the phase is calculated from measurements obtained through numerical simulation of a one-dimensional FHN reactiondiffusion model, which is described in this section.

In the model used in the numerical simulation, the variable r in Eq. (1) is replaced with x, representing a point in onedimensional space. The state variable, diffusion coefficient, local reaction dynamics, and the mutual coupling in Eq. (1) are defined as follows:

$$X_{i}(x,t) = \begin{pmatrix} u_{i} \\ v_{i} \end{pmatrix},$$

$$F_{i}(X_{i},x) = \begin{pmatrix} u_{i}(u_{i} - \alpha)(1 - u_{i}) - v_{i} \\ \tau_{i}^{-1}(u_{i} - \gamma v_{i}) \end{pmatrix},$$

$$D_{i} = \begin{pmatrix} \kappa_{i} & 0 \\ 0 & \delta_{i} \end{pmatrix}, \quad G(X_{i}, X_{j}) = K \begin{pmatrix} u_{j} - u_{i} \\ v_{j} - v_{i} \end{pmatrix}, \quad (2$$

where $u_i = u_i(x,t)$ and $v_i = v_i(x,t)$ are activator and inhibitor variables, respectively. We denote the limit-cycle solution of the model without mutual coupling (G = 0) as $\chi_i(x, \phi_i) = (\chi_{u_i}(x,\phi_i),\chi_{v_i}(x,\phi_i))$. The spatiotemporal dynamics can exhibit various typical patterns, such as circulating pulses on a ring, oscillating spots, target waves, and rotating spirals by setting the parameters α , τ_i , γ_i , and the diffusion coefficient κ_i and δ_i appropriately [75–78]. The parameter $\alpha = \alpha(x)$ is space dependent.

In this study, we simulate rhythmic patterns of target waves. (In Appendix G, the model exhibiting oscillating spots is explained.) To create a pacemaker region of target waves, the parameter α is assumed to possess heterogeneity, i.e., $\alpha(x) = \alpha_0 + (\alpha_1 - \alpha_0) \exp(-r^4/r_0^4)$, where $r = |x - x_0|$ represents the distance from the center of the pacemaker region, and r_0 is the pacemaker region's radius. Specifically, $\alpha(x) \rightarrow$ α_1 as $r \to 0$, and $\alpha(x) \to \alpha_0$ as $r \to \infty$. The parameters defining the pacemaker region are $r_0 = 10$, $x_0 = 80$, $a_0 = 0.1$, and $a_1 = -0.1$. Other parameters are $\gamma = 2.5$, $\tau_1^{-1} = 0.005$, $\tau_2^{-1} = 0.0055$, $\kappa_1 = \kappa_2 = 0.15$, and $\delta_1 = \delta_2 = 0$. The periods of the limit-cycle solutions are $T_1 \simeq 204.6$ and $T_2 \simeq$ 189.4. The coupling intensity is $K = \text{diag}(5.0 \times 10^{-4}, 0)$. For the numerical simulation, we used a one-dimensional system of size L = 100 with no-flux boundary conditions. The system is discretized into spatial grids with $\Delta x = L/2^8$.

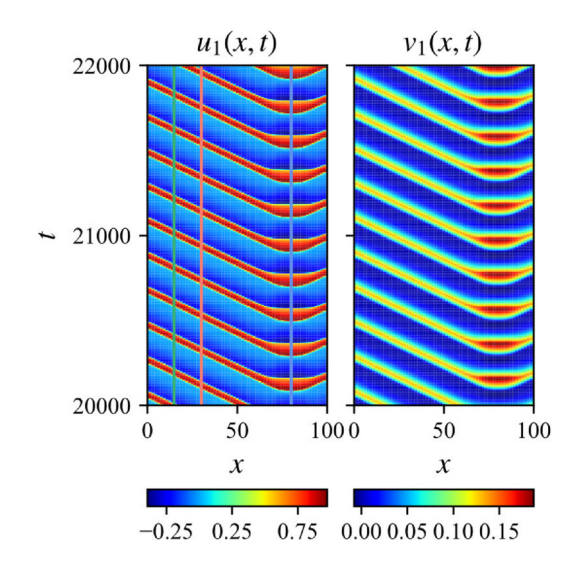


FIG. 1. Spatiotemporal dynamics of the target waves simulated by the coupled FHN reaction-diffusion models. For reference, the green, red, and blue vertical lines mark the measurement positions, $x_p \simeq 15, 30, 80$, respectively (see Sec. IV C).

Time integration begins from spatially uniform initial conditions $u_1(x,0) = 0.180$, $v_1(x,0) = 0.004$, $u_2(x,0) = 0.463$, and $v_2(x,0) = 0.145$. The initial time evolution up to 5.0×10^4 is discarded, and measurements are taken from the subsequent evolution over a duration of 3.0×10^5 . (We designate the start of measurements as t = 0 hereafter.) Time integration was performed using the explicit Heun scheme with a time step $\Delta t = 0.01$.

Figure 1 shows the spatiotemporal dynamics of u_1 and v_1 . The pacemaker region with radius r_0 and center $x=x_0$ is self-oscillatory and rhythmically emits target waves. The waves propagate from the pacemaker region outward through the excitable surrounding area. In addition, the limit-cycle solution is depicted in Fig. 8(a) in Appendix C, and Fig. 8(b) in Appendix C shows the phase sensitivity function, $Q_i(x, \phi_i) = (Q_{u_i}(x, \phi_i), Q_{v_i}(x, \phi_i))$, which quantifies linear response characteristics of the phase to weak perturbation. The phase sensitivity function is localized at the pacemaker region (near x = 80), indicating that this region primarily influences the rhythm of the entire system.

IV. CALCULATING THE PHASE FROM A MEASUREMENT ON A SINGLE SPATIAL GRID POINT

This section presents the method for phase calculation that uses a Poincaré section applied to measurement time series of spatiotemporal dynamics at a fixed position. We begin by outlining the linear interpolation technique for phase calculation (Sec. IV A) and the approach for selecting an optimal measurement position to ensure accuracy (Sec. IV B). Following this, we illustrate the phase calculation method through a numerical simulation of the FHN reaction-diffusion model, which features target waves (Sec. IV C). Additionally, in Appendix G, we applied the same approach to spatiotemporal dynamics exhibiting oscillating spots.

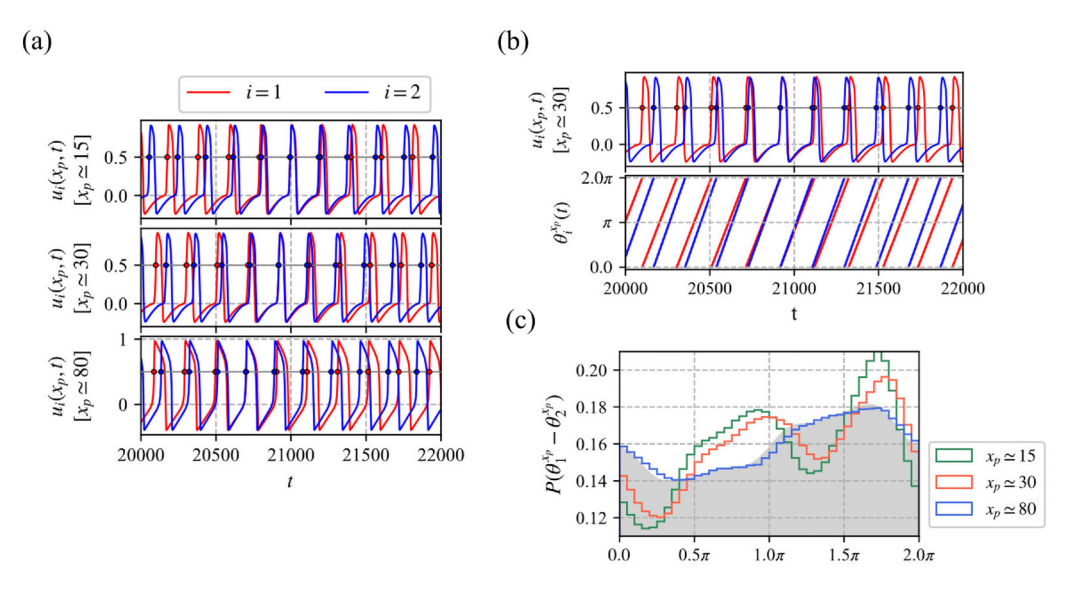


FIG. 2. Time series of $u_i(x_p,t)$ and the calculation of $\theta_i^{x_p}(t)$. (a) Time series of $u_i(x_p,t)$ and the Poincaré sections for $x_p \simeq 15$, 30, 80. The red and blue lines indicate i=1 and i=2, respectively. The horizontal lines depict the Poincaré sections, and the dots represent the times at which $u_i(x_p,t)$ intersects the Poincaré section from negative to positive. (b) Example of the calculation of $\theta_i^{x_p}(t)$ for $x_p \simeq 30$. The red and blue colors indicate i=1 and i=2, respectively. (Top) Recording the time of intersection. The dots represent the time $t_{i,j}^{x_p}$. (Bottom) Calculation of the time series of $\theta_i^{x_p}(t)$ using the linear interpolation [see Eq. (3)]. The phase increases linearly by 2π during $t_{i,j+1}^{x_p} - t_{i,j}^{x_p}$. (c) Histograms of $\theta_i^{x_p} - \theta_j^{x_p}$ for $x_p \simeq 15$ (green), 30 (red), and 80 (blue). The histograms are calculated over a duration in which $|\theta_i^{x_p} - \theta_j^{x_p}|$ increases by 200π . The distribution calculated from the phase equations is displayed in gray.

A. Phase calculation by linear interpolation

We calculate the phase by applying a Poincaré section to the time series of $u_i(x_p,t)$, which is measured at a specific spatial grid point of $x=x_p$. Let us consider an example of spatiotemporal dynamics exhibiting target waves (Sec. III). Figure 2(a) shows the time series of $u_i(x_p,t)$ measured at $x_p \simeq 15$, 30, 80. As shown in this figure, the Poincaré sections are applied to each time series, recording the time $t_{i,j}^{x_p}$ when $u_i(x_p,t)$ intersects the Poincaré section (from negative to positive) for the jth time. The phase $\theta_i^{x_p}$ is then calculated from the set of times $\{t_{i,j}^{x_p}\}_j$ ensuring that it satisfies $\theta_{i,j}^{x_p}(t_{i,j}^{x_p}) = 2\pi j$. To make the time series of $\theta_i^{x_p}(t)$, we employ linear interpolation of the phase as follows:

$$\theta_i^{x_p}(t) = 2\pi j + 2\pi \frac{t - t_{i,j}^{x_p}}{t_{i,j+1}^{x_p} - t_{i,j}^{x_p}} \quad (t_{i,j}^{x_p} \leqslant t \leqslant t_{i,j+1}^{x_p}).$$
 (3)

Figure 2(b) presents the time series of $\theta_i^{x_p}$ calculated from the time series of $u_i(x_p, t)$ for $x_p \simeq 30$. The interval of the time grid for the interpolation is 0.1. Figure 2(c) shows histograms of $\theta_1^{x_p}(t) - \theta_2^{x_p}(t)$ for $x_p \simeq 15$, 30, 80. The figure indicates the dependency of $\theta_i^{x_p}$ on x_p . Specifically, the histograms vary with changes in x_p , indicating that the calculated phase θ_i depends on the measurement position. However, according to phase reduction theory, these phases should ideally remain independent of the measurement position.

B. Approach to determine the position to measure

We introduce the isochron-based phase $\phi_i(t)$ to elucidate the dependency of the calculated phase $\theta_i^{x_p}$ on x_p and outline an approach for accurately calculating the phases. Generally,

there is a difference between the two phases, $\theta_i^{x_p}$ and ϕ_i , which can be evaluated using a linear approximation near the limit-cycle solution. (The method for calculating the phase using the linear approximation in the ODE case is described in Appendix A, while the corresponding approach for the PDE case is described in Appendix B.) Here, let us consider the general reaction-diffusion model described in Eq. (1). We assume that a Poincaré section is applied to the time series of $X_{i,n_p}(x_p,t)$, which is the n_p th entry of $X_i(x_p,t)$. We record the time $t_{i,j}^{x_p}$ when $X_{i,n_p}(x_p,t)$ intersects the Poincaré section for the jth time. The phase time series is then calculated using Eq. (3). Using the phase sensitivity function $Q_i(x,\phi_i) \in \mathbb{R}^N$, which quantifies linear response characteristics of the phase to weak perturbations, $\phi_i(t_{i,j}^{x_p})$ is calculated from $\theta_i^{x_p}(t_{i,j}^{x_p})$ as follows:

$$\phi_{i}(t_{i,j}^{x_{p}}) = \theta_{i}^{x_{p}}(t_{i,j}^{x_{p}}) + c_{i,j}^{x_{p}} = 2\pi j + c_{i,j}^{x_{p}},$$

$$c_{i,j}^{x_{p}} = \sum_{\substack{(m,n) \\ \neq (m_{p},n_{p})}}^{(M,N)} Q_{i,n}(x_{m}, 0) \Delta_{i,n}(x_{m}, t_{i,j}^{x_{p}}) \Delta x_{m},$$

$$\Delta_{i,n}(x, t_{i,j}^{x_p}) := X_{i,n}(x, t_{i,j}^{x_p}) - \chi_{i,n}(x, 0),$$

$$\Delta x_m := \begin{cases} \Delta x/2 & (m = 0, M), \\ \Delta x & (\text{otherwise}), \end{cases}$$
(4)

where $X_{i,n}(x_m, t_{i,j}^{x_p})$, $\chi_{i,n}(x_m, 0)$, and $Q_{i,n}(x_m, 0)$ are the nth entry of $X_i(x_m, t_{i,j}^{x_p})$, $\chi_i(x_m, 0)$, and $Q_i(x_m, 0)$, respectively, and $\Delta_{i,n}$ is the deviation of $X_{i,n}$ from the state of $\phi_i = 0$ on the limit-cycle solution. We assume that $\chi_i(x_m, 0)$ is specified at the intersection of the limit-cycle solution and the Poincaré section. The integration about x is expressed by discrete representation with the spatial grid $x_m = m\Delta x$ (m = 0, 1, ..., M)

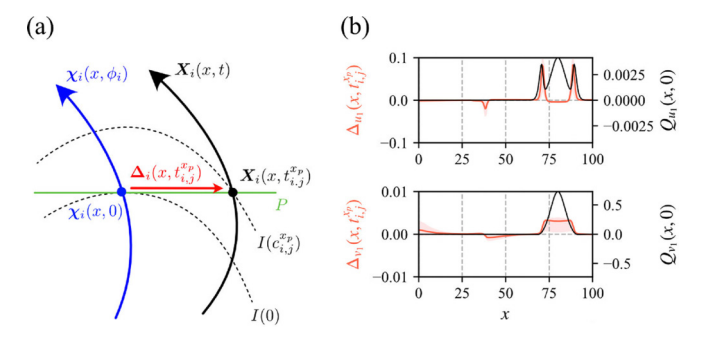


FIG. 3. Illustration of calculation of the correction terms. [Fig. 3(b) is identical to some of the contents in Fig. 4(a).] (a) Illustration of two states on the same Poincaré section. The two states, $\chi_i(x, 0)$ and $X_i(x, t_{i,j}^{x_p})$, lie on the same Poincaré section P but on different isochrons, I(0) and $I(c_{i,j}^{x_p})$, respectively. The difference between these states is represented as $\Delta_i(x, t_{i,j}^{x_p})$, whose nth entry is denoted as $\Delta_{i,n}$ used in Eq.(4). These states are located on distinct isochrons unless the Poincaré section is the same as I(0). The correction term quantifies the difference between the phases assigned to these distinct isochrons. (b) Distributions of $\Delta_{u_1}(x, t_{1,j}^{x_p})$ and $\Delta_{v_1}(x, t_{1,i}^{x_p})$ under the condition of $x_p \simeq 30$, along with the phase sensitivity functions, $Q_{u_1}(x, 0)$ and $Q_{v_1}(x, 0)$, for the spatiotemporal dynamics simulated by the FHN reaction-diffusion model. The top figure displays $\Delta_{u_1}(x, t_{1,j}^{x_p})$ and $Q_{u_1}(x, 0)$, and the bottom figure displays $\Delta_{v_1}(x, t_{1,j})$ and $Q_{v_1}(x, 0)$. The red lines indicate the medians of $\Delta_{u_1}(x, t_{1,j}^{x_p})$ and $\Delta_{v_1}(x, t_{1,j}^{x_p})$. The red shades indicate the range between the 25th and 75th percentiles. The black lines indicate $Q_{u_1}(x,0)$ and $Q_{v_1}(x,0)$.

that satisfies $x_{m_p} = x_p$ and $x_M = L$. The entry of (m_p, n_p) are removed from the summation in Eq. (4) since the two values, $X_{i,n_p}(x_p, t_{i,j}^{x_p})$ and $\chi_{i,n_p}(x_p, 0)$, have the same value on the Poincaré section, i.e., $\Delta_{i,n_p}(x_{m_p}, t_{i,j}^{x_p}) = 0$. We call the variable $c_{i,j}^{x_p}$, which represents the difference between $\theta_i^{x_p}(t_{i,j}^{x_p})$ and $\phi_i(t_{i,j}^{x_p})$, the correction term. Figure 3(a) explains how the correction term occurs. The figure illustrates that the two states, $\chi_i(x,0)$ and $X_i(x,t_{i,j}^{x_p})$, lie on the same Poincaré section P but on different isochrons, I(0) and $I(c_{i,j}^{x_p})$. Generally, these states are located on distinct isochrons unless the Poincaré section is the same as I(0). The correction term accounts for the difference between the phases associated with the two isochrons.

We rewrite Eq. (4) for the FHN reaction-diffusion model as follows:

$$\phi_{i}(t_{i,j}^{x_{p}}) = 2\pi j + c_{i,j}^{x_{p}},$$

$$c_{i,j}^{x_{p}} = \sum_{m \neq m_{p}}^{M} Q_{u_{i}}(x_{m}, 0) \Delta_{u_{i}}(x_{m}, t_{i,j}^{x_{p}}) \Delta x_{m}$$

$$+ \sum_{m=0}^{M} Q_{v_{i}}(x_{m}, 0) \Delta_{v_{i}}(x_{m}, t_{i,j}^{x_{p}}) \Delta x_{m},$$

$$\Delta_{u_{i}}(x, t_{i,j}^{x_{p}}) := u_{i}(x, t_{i,j}^{x_{p}}) - \chi_{u_{i}}(x, 0),$$

$$\Delta_{v_{i}}(x, t_{i,j}^{x_{p}}) := v_{i}(x, t_{i,j}^{x_{p}}) - \chi_{v_{i}}(x, 0),$$

$$\Delta x_{m} := \begin{cases} \Delta x/2 & (m = 0, M), \\ \Delta x & (\text{otherwise}), \end{cases}$$
(5)

where $Q_{u_i}(x, \phi_i)$ and $Q_{v_i}(x, \phi_i)$ are the phase sensitivity functions of u_i and v_i , respectively, and Δ_{u_i} and Δ_{v_i} are the deviations of u_i and v_i from the state of $\phi_i = 0$ on the limit-cycle solution, respectively. The subscript n used in Eq. (4) is removed since the entry of two-dimensional state (n = 1, 2) is represented by variable u_i and v_i . Additionally, the subscript n_p is removed since the Poincaré section applied solely to the time series of $u_i(x_p, t)$. We then proceed to linearly interpolate the phase $\phi_i(t)$ as follows:

$$\phi_{i}(t) = \phi_{i}(t_{i,j}^{x_{p}}) + (\phi_{i}(t_{i,j+1}^{x_{p}}) - \phi_{i}(t_{i,j}^{x_{p}})) \frac{t - t_{i,j}^{x_{p}}}{t_{i,j+1}^{x_{p}} - t_{i,j}^{x_{p}}}$$

$$= 2\pi j + c_{i,j}^{x_{p}} + (2\pi + c_{i,j+1}^{x_{p}} - c_{i,j}^{x_{p}}) \frac{t - t_{i,j}^{x_{p}}}{t_{i,j+1}^{x_{p}} - t_{i,j}^{x_{p}}}$$

$$(t_{i,i}^{x_{p}} \leq t \leq t_{i,i+1}^{x_{p}}). \tag{6}$$

The transformation to the second row is achieved by substituting Eq. (5) into the first row. Similar to the interpolation process for $\theta_i^{x_p}(t)$ described in Eq. (3), the time grid interval for this interpolation is set to 0.1.

The correction terms are influenced by the two factors: (i) deviation from the limit-cycle solution and (ii) heterogeneity of the amplitude of the phase sensitivity function. Let us consider the calculation of $\theta_i^{x_p}$ for spatiotemporal dynamics numerically simulated by the FHN reaction-diffusion model (Sec. III). For example, we use the measurement time series of $u_i(x_p, t)$ under the condition of $x_p \simeq 30$. Figure 3(b) displays the distribution of $\Delta_{u_i}(x, t_{i,j}^{x_p})$ and $\Delta_{v_i}(x, t_{i,j}^{x_p})$, which is recorded at time $t_{i,j}^{x_p}$ when the measurement time series intersects the Poincaré section, alongside $Q_{u_i}(x, 0)$ and $Q_{v_i}(x, 0)$. The figure indicates that the region with large $|\Delta_{u_i}(x, t_{i,j}^{x_p})|$ and $|\Delta_{v_i}(x, t_{i,j}^{x_p})|$ overlaps the region with large $|Q_{u_i}(x, 0)|$ and $|Q_{v_i}(x,0)|$. In such a case, the magnitude of $c_{i,i}^{x_p}$ is supposed to be large according to Eq. (5). This overlap can be avoided by setting x_p appropriately since the region with large $|\Delta_{u_i}(x, t_{i,j}^{x_p})|$ and $|\Delta_{v_i}(x, t_{i,j}^{x_p})|$ varies with x_p . Specifically, $|\Delta_{u_i}(x, t_{i,j}^{x_p})|$ and $|\Delta_{v_i}(x, t_{i,j}^{x_p})|$ near x_p are almost zero. Therefore, a strategy to reduce the magnitude of $c_{i,j}^{x_p}$ is to choose x_p within the region where the amplitudes of the phase sensitivity functions are large. It is known that the phase sensitivity function is localized at the pacemaker region of target waves [56].

C. Example

We illustrate the approach for reducing the magnitude of $c_{i,j}^{x_p}$ using the numerical simulation with the FHN reaction-diffusion model. The time series of $\theta_i^{x_p}(t)$ and $\phi_i(t)$, spanning a duration of 3.0×10^5 , are calculated from measurements obtained from the simulation (Sec. III). Simultaneously, $\Delta_{u_i}(x,t_{i,j}^{x_p})$, $\Delta_{v_i}(x,t_{i,j}^{x_p})$, and corresponding $c_{i,j}^{x_p}$ are obtained for each $t_{i,j}^{x_p}$. The results of the phase calculation are compared for each measurement position x_p . For a detailed explanation, the distribution of $\Delta_{u_i}(x,t_{i,j}^{x_p})$ and $\Delta_{v_i}(x,t_{i,j}^{x_p})$ and the statistics of $c_{i,j}^{x_p}$ are also shown.

Figure 1 shows the spatiotemporal dynamics exhibiting target waves. We calculated the time series of $\theta_i^{x_p}(t)$ from

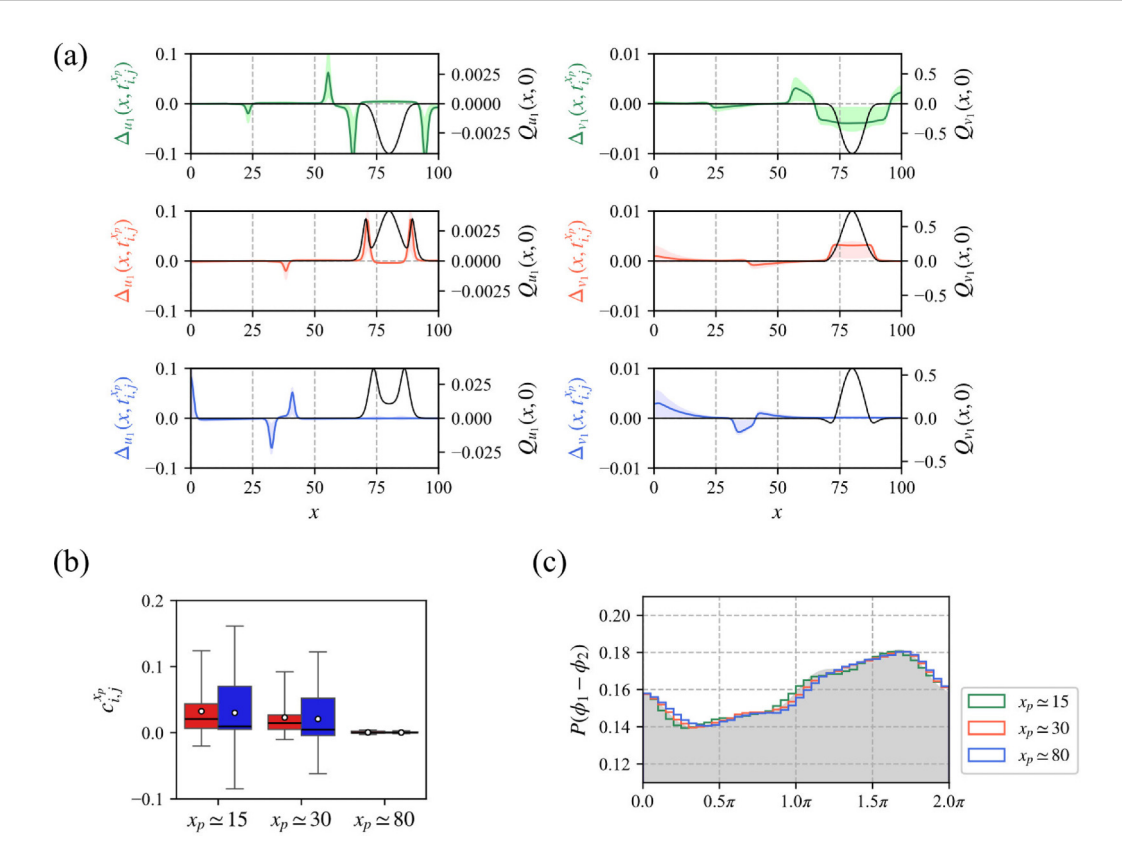


FIG. 4. Calculation of the correction terms and the phase from measurements taken at a single spatial grid point. (a) Distribution of $\Delta_{u_1}(x, t_{1,j}^{x_p})$ and $\Delta_{v_1}(x, t_{1,j}^{x_p})$ under the condition of $x_p \simeq 15$ (top), 30 (middle), and 80 (bottom), along with the phase sensitivity functions, $Q_{u_1}(x, 0)$ and $Q_{v_1}(x, 0)$, for the spatiotemporal dynamics simulated by the FHN reaction-diffusion model. The left figures display $\Delta_{u_1}(x, t_{1,j}^{x_p})$ and $Q_{u_1}(x, 0)$, and the right figures display $\Delta_{v_1}(x, t_{1,j})$ and $Q_{v_1}(x, 0)$. The colored lines indicate the medians of $\Delta_{u_1}(x, t_{1,j}^{x_p})$ and $\Delta_{v_1}(x, t_{1,j}^{x_p})$. The colored shades indicate the range between the 25th and 75th percentiles. The black lines indicate $Q_{u_1}(x, 0)$ and $Q_{v_1}(x, 0)$. (b) Statistics of the correction term $c_{i,j}^{x_p}$ for $x_p \simeq 15$, 30, 80. The red (i = 1) and blue (i = 2) boxes represent the first and third quartiles of dataset $\{c_{i,j}^{x_p}\}_j$. The horizontal lines mark the medians, while the dots mark the averages. The whiskers extend to show the maximum and minimum values. (c) Histograms of $\phi_1 - \phi_2$ for $x_p \simeq 15$ (green), 30 (red), and 80 (blue). The histograms are calculated over a duration in which $|\phi_1 - \phi_2|$ increases by 200π . The distribution calculated from the phase equations is displayed in gray.

that of $u_i(x_p, t)$ for $x_p \simeq 15$, 30, 80 (the exact values are $x_p = 38\Delta x$, $77\Delta x$, $205\Delta x$). Only $x_p \simeq 80$ belongs to the pacemaker region. Examples of the time series of $u_i(x_p, t)$ and the Poincaré section for each x_p are shown in Fig. 2(a). Figure 2(c) shows that the histograms of $\theta_1^{x_p} - \theta_2^{x_p}$ vary with x_p . The difference between the histogram of $\theta_1^{x_p} - \theta_2^{x_p}$ and the distribution of $\phi_1 - \phi_2$, calculated from the phase equations (Appendix D), is minimal for $x_p \simeq 80$. Therefore, the approach described in Sec. IV B appears to be effective.

To verify the effectiveness of the approach, we refer to Fig. 4(a), which shows the distribution of $\Delta_{u_i}(x, t_{i,j}^{x_p})$ and $\Delta_{v_i}(x, t_{i,j}^{x_p})$, along with $Q_{u_i}(x, 0)$ and $Q_{v_i}(x, 0)$. The region with large $|\Delta_{u_i}(x, t_{i,j}^{x_p})|$ does not overlap the region with large $|Q_{u_i}(x, 0)|$ for $x_p \simeq 80$ although the two regions overlap for $x_p \simeq 15$, 30 (the same is true for Q_{v_i} and Δ_{v_i}). Given this result, the magnitude of the correction term is relatively small for $x_p \simeq 80$ and larger for the other x_p . The statistics of the correction term indicate that the correction term is close to zero only for $x_p \simeq 80$ [Fig. 4(b)]. From these results, our method successfully operated as intended.

Ignoring the correction term impacts the phase calculation results, with the extent of the impact varying according to the magnitude of the correction term. Figure 4(c) shows the histograms of $\phi_1 - \phi_2$ calculated on the basis of Eqs. (5) and (6). The histograms of $\phi_1 - \phi_2$ for $x_p \simeq 15, 30, 80$ are almost similar, although the histogram of $\theta_1^{x_p} - \theta_2^{x_p}$ shown in Fig. 2(c) varies with x_p . It is evident that the histograms of $\theta_1^{x_p} - \theta_2^{x_p}$ and $\phi_1 - \phi_2$ differ significantly for $x_p \simeq 15, 30$ since the magnitude of the correction term is large, whereas they are similar for $x_p \simeq 80$ since the correction term is nearly zero. Ignoring the correction term degrades the accuracy of phase equation estimation when x_p is not appropriate. Figures 9(a) and 9(b) in Appendix E show the phase equations estimated from the time series of $\theta_i^{x_p}(t)$ and $\phi_i(t)$, respectively. The phase equations estimated from $\theta_i^{x_p}$ deviate significantly from the true forms for $x_p \simeq 15, 30$, but closely match the true forms for $x_p \simeq 80$. In contrast, the phase equations estimated from ϕ_i are consistent with the true forms regardless of x_p . Appendix G shows that this approach is also effective for oscillating spots.

V. CALCULATING THE PHASE FROM MEASUREMENTS ON ALL SPATIAL GRID POINTS

We explore a method for calculating the phase using the Poincaré section applied to time series obtained by the orthogonal decomposition of the spatiotemporal dynamics. The orthonormal basis functions used in this decomposition are assumed to be obtained through PCA (see, e.g., Ref. [74]). We explain the orthogonal decomposition technique (Sec. V A), the linear interpolation to calculate the phase (Sec. V B), and the differences between the calculated phase and isochron-based phase (Sec. V C). Then, we illustrate the phase calculation for spatiotemporal dynamics using two different decomposition schemes (Secs. V D and V E). In addition, we apply the same schemes to spatiotemporal dynamics exhibiting oscillating spots (Appendix G).

A. Orthogonal decomposition

Before delving into the specifics of the FHN reaction-diffusion model, we consider the general form of the reaction-diffusion model described by Eq. (1). The *n*th entries of the state vector X_i , limit-cycle solution χ_i , and phase sensitivity function Q_i are represented as $X_{i,n}$, $\chi_{i,n}$, and $Q_{i,n}$, respectively. For decomposition, we project them onto the orthonormal basis functions $\Phi_{i,n}^k(k=1,2,\ldots,K)$ as follows:

$$X_{i,n}^{k}(t) = \int_{0}^{L} X_{i,n}^{k}(x,t) \Phi_{i,n}^{k}(x) dx,$$

$$\chi_{i,n}^{k}(\phi_{i}) = \int_{0}^{L} \chi_{i,n}^{k}(x,\phi_{i}) \Phi_{i,n}^{k}(x) dx,$$

$$Q_{i,n}^{k}(\phi_{i}) = \int_{0}^{L} Q_{i,n}^{k}(x,\phi_{i}) \Phi_{i,n}^{k}(x) dx,$$
(7)

where the basis function satisfies $\int_0^L \Phi_{i,n}^p(x) \Phi_{i,n}^q(x) dx = \delta_{pq}$ (δ_{pq} denotes the Kronecker delta). According to Eq. (7), the infinite-dimensional state space is mapped to KN-dimensional state space.

We rewrite Eq. (7) for the FHN reaction-diffusion model. Given the orthonormal basis functions $\Phi_{u_i}^k(x)$ (k = 1, 2, ..., K), the projections of the state variable, limit cycle solution, and phase sensitivity function associated with u_i onto the basis functions are calculated as follows:

$$u_{i}^{k}(t) = \int_{0}^{L} u_{i}(x, t) \Phi_{u_{i}}^{k}(x) dx,$$

$$\chi_{u_{i}}^{k}(\phi_{i}) = \int_{0}^{L} \chi_{u_{i}}(x, \phi_{i}) \Phi_{u_{i}}^{k}(x) dx,$$

$$Q_{u_{i}}^{k}(\phi_{i}) = \int_{0}^{L} Q_{u_{i}}(x, \phi_{i}) \Phi_{u_{i}}^{k}(x) dx,$$
(8)

where the basis functions satisfies $\int_0^L \Phi_{u_i}^p(x) \Phi_{u_i}^q(x) \mathrm{d}x = \delta_{pq}$. The variables $v_i^k(t)$, $\chi_{v_i}^k(\phi_i)$, and $Q_{v_i}^k(\phi_i)$ are similarly calculated using the orthonormal basis functions $\Phi_{v_i}^k(x)$ (the equations are abbreviated). In Sec. VD, we investigate a scheme that applies PCA to measurements u_i and v_i collected across all spatial grid points to obtain the basis functions. In Sec. VE, we propose an alternative scheme in which PCA is applied directly to the phase sensitivity functions. We set

K = 50 or K = 200 to ensure that each function can be reproduced nearly 100% on the basis of the following equations:

$$u_{i}(x,t) \simeq \sum_{k=1}^{K} u_{i}^{k}(t) \Phi_{u_{i}}^{k}(x),$$

$$\chi_{u_{i}}(x,\phi_{i}) \simeq \sum_{k=1}^{K} \chi_{u_{i}}^{k}(\phi_{i}) \Phi_{u_{i}}^{k}(x),$$

$$Q_{u_{i}}(x,\phi_{i}) \simeq \sum_{k=1}^{K} Q_{u_{i}}^{k}(\phi_{i}) \Phi_{u_{i}}^{k}(x).$$
(9)

The variables $v_i(x, t)$, $\chi_{v_i}(x, \phi_i)$, and $Q_{v_i}(x, \phi_i)$ are calculated in a similar way (the equations are abbreviated).

B. Phase calculation by linear interpolation

We calculate the phase $\theta_i^{k_p}$ from the time series of $u_i^{k_p}(x,t)$ or $v_i^{k_p}(x,t)$. The Poincaré section is applied to the time series of $u_i^{k_p}(t)$ or $v_i^{k_p}(t)$, recording the time $t_{i,j}^{k_p}$ when the time series intersects the Poincaré section for the jth time. The phase $\theta_i^{k_p}$ is then calculated from the set of times, $\{t_{i,j}^{k_p}\}_j$, ensuring that it satisfies $\theta_{i,j}^{k_p}(t_{i,j}^{k_p}) = 2\pi j$. As in Eq. (3), we employ linear interpolation of the phase as follows:

$$\theta_i^{k_p}(t) = 2\pi j + 2\pi \frac{t - t_{i,j}^{k_p}}{t_{i,j+1}^{k_p} - t_{i,j}^{k_p}} \quad \left(t_{i,j}^{k_p} \leqslant t \leqslant t_{i,j+1}^{k_p}\right). \tag{10}$$

We assume $k_p = 1$, and using another variable, $u_i^{k_p}(t)$ or $v_i^{k_p}(t)$ $(k_p \ge 2)$, is not discussed in this study.

C. Difference between the calculated phase and isochron-based phase

We calculated the isochron-based phase $\phi_i(t)$, which obeys the isochron deformed by the orthogonal decomposition. There is a difference between the phases, $\theta_i^{k_p}$ and ϕ_i , which can be evaluated using a linear approximation in the vicinity of the limit-cycle solution. Let us consider the general form of the reaction-diffusion model described in Eq. (1). We assume that the Poincaré section is applied to the time series of $X_{i,n_p}^{k_p}$ and that the time $t_{i,j}^{k_p}$ is recorded when $X_{i,n_p}^{k_p}(t)$ intersects the Poincaré section for the jth time. The time series of the phase $\theta_i^{k_p}$ is calculated using Eq. (10). We then define the correction term $c_{i,j}^{k_p}$ as the difference between $\theta_i^{k_p}(t_{i,j}^{k_p})$ and $\phi_i(t_{i,j}^{k_p})$. The phase $\phi_i(t_{i,j}^{k_p})$ and correction term are calculated as follows:

$$\phi_{i}(t_{i,j}^{k_{p}}) = \theta_{i}^{k_{p}}(t_{i,j}^{k_{p}}) + c_{i,j}^{k_{p}} = 2\pi j + c_{i,j}^{k_{p}},$$

$$c_{i,j}^{k_{p}} = \sum_{(k,n)\neq(k_{p},n_{p})}^{(K,N)} Q_{i,n}^{k}(0)\Delta_{i,n}^{k}(t_{i,j}^{k_{p}}),$$

$$\Delta_{i,n}^{k}(t_{i,j}^{k_{p}}) := X_{i,n}^{k}(t_{i,j}^{k_{p}}) - \chi_{i,n}^{k}(0),$$
(11)

where $\Delta_{i,n}^k$ is the deviations of $X_{i,n}^k$ from the state of $\phi_i = 0$ on the limit-cycle $\chi_{i,n}^k$. The entry of (k_p, n_p) are removed from

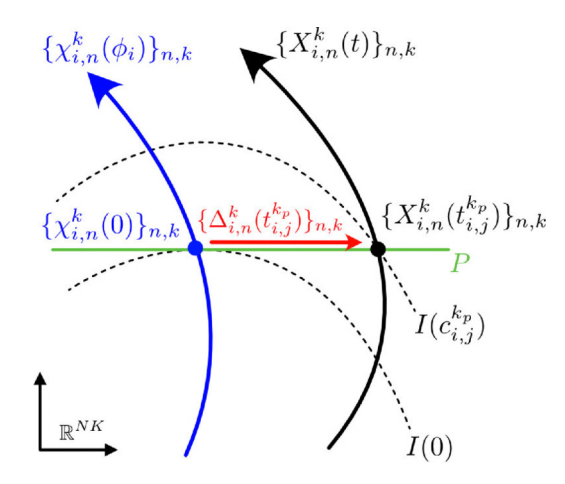


FIG. 5. Illustration of two states on the same Poincaré section. We consider the isochron mapped from an infinite-dimensional space to a KN-dimensional space. The two states, $\{\chi_{i,n}^k(0)\}_{n,k}$ and $\{X_{i,n}^k(t_{i,n}^{k_p})\}_{n,k}$, lie on the same Poincaré section P but on different isochrons, I(0) and $I(c_{i,j}^{k_p})$, respectively. The difference between these states is represented as $\{\Delta_{i,n}^k(t_{i,j}^{k_p})\}_{n,k}$ used in Eq. (11). These states are located on distinct isochrons unless the Poincaré section is the same as I(0). The correction term quantifies the difference between the phases assigned to these distinct isochrons.

the summation in Eq. (11) since the two values, $X_{i,n_p}^{k_p}(t_{i,j}^{k_p})$ and $\chi_{i,n_p}^{k_p}(0)$, are equal on the Poincaré section, i.e., $\Delta_{i,n_p}^{k_p}(t_{i,j}^{k_p})=0$. The derivation of Eq. (11) is detailed in Appendix F. Figure 5 illustrates that the two states in the KN-dimensional space, $\{\chi_{i,n}^k(0)\}_{n,k}$ and $\{X_{i,n}^k(t_{i,j}^{k_p})\}_{n,k}$, lie on the same Poincaré section P but on different isochrons, I(0) and $I(c_{i,j}^{k_p})$. Note that the isochron is mapped from the infinite-dimensional space to the KN-dimensional space through orthogonal decomposition. Unless the Poincaré section is the same as I(0), the two states are located on distinct isochrons. The correction term represents the difference between the phases associated with these two isochrons.

We rewrite Eq. (11) for the FHN reaction-diffusion model. Here, we use the index $n_p \in \{u, v\}$ to denote whether the Poincaré section is applied to the time series of u_i^1 or v_i^1 , instead of $1 \le n_p \le N$ used in Eq. (11). When we apply the Poincaré section to the time series of $u_i^{k_p}$, i.e., $n_p = u$, the phase $\phi_i(t_{i,j}^{k_p})$ and correction term are calculated as follows:

$$\phi_{i}(t_{i,j}^{k_{p}}) = 2\pi j + c_{i,j}^{k_{p}},$$

$$c_{i,j}^{k_{p}} = \sum_{k \neq k_{p}}^{K} Q_{u_{i}}^{k}(0) \Delta_{u_{i}}^{k}(t_{i,j}^{k_{p}}) + \sum_{k=1}^{K} Q_{v_{i}}^{k}(0) \Delta_{v_{i}}^{k}(t_{i,j}^{k_{p}}), \quad (12)$$

where $\Delta_{u_i}^k(t_{i,j}^{k_p}) := u_i^k(t_{i,j}^{k_p}) - \chi_{u_i}^k(0)$ and $\Delta_{v_i}^k(t_{i,j}^{k_p}) := v_i^k(t_{i,j}^{k_p}) - \chi_{v_i}^k(0)$ are the deviations of u_i^k and v_i^k from the state of $\phi_i = 0$ on the limit-cycle solution. When the Poincaré section is applied to the time series of $v_i^{k_p}$, i.e., $n_p = v$, the correction

term is calculated as follows instead of Eq. (12):

$$c_{i,j}^{k_p} = \sum_{k=1}^{K} Q_{u_i}^k(0) \Delta_{u_i}^k(t_{i,j}^{k_p}) + \sum_{k \neq k_n}^{K} Q_{v_i}^k(0) \Delta_{v_i}^k(t_{i,j}^{k_p}).$$
 (12')

Hereafter, when we refer to Eq. (12), Eq. (12)' is also included to the reference implicitly. Then, we linearly interpolate the phase as follows:

$$\phi_{i}(t) = \phi_{i}(t_{i,j}^{k_{p}}) + (\phi_{i}(t_{i,j+1}^{k_{p}}) - \phi_{i}(t_{i,j}^{k_{p}})) \frac{t - t_{i,j}^{k_{p}}}{t_{i,j+1}^{k_{p}} - t_{i,j}^{k_{p}}}$$

$$= 2\pi j + c_{i,j}^{k_{p}} + (2\pi + c_{i,j+1}^{k_{p}} - c_{i,j}^{k_{p}}) \frac{t - t_{i,j}^{k_{p}}}{t_{i,j+1}^{k_{p}} - t_{i,j}^{k_{p}}}$$

$$(t_{i,j}^{k_{p}} \leqslant t \leqslant t_{i,j+1}^{k_{p}}). \tag{13}$$

The transformation to the second row is achieved by substituting Eq. (12) into the first row. According to Eq. (11) or (12), the magnitude of the correction term depends on both the deviation magnitude from the limit-cycle solution and the amplitude of the (decomposed) phase sensitivity functions. Therefore, when u_i^k or v_i^k fluctuates significantly and the corresponding $Q_{u_i}^k$ or $Q_{v_i}^k$ has a large amplitude, the magnitude of the correction term becomes large. We present the results of phase calculations for both $n_p = u$ and $n_p = v$, but selecting n_p does not inherently improve the accuracy of the phase calculation.

D. Case of using the basis function obtained from the spatiotemporal dynamics

We illustrate the process of phase calculation for spatiotemporal dynamics using the numerical simulation with the FHN reaction-diffusion model (Sec. III). We assume that the basis functions, $\Phi^k_{u_i}$ and $\Phi^k_{v_i}$, are derived by solving eigenproblems for the covariance matrices of the measurements $u_i(x,t)$ and $v_i(x,t)$, respectively. The temporal means of the measurements are defined as $\overline{u_i}(x) := \sum_{s=1}^S u_i(x,t_s)/S$ and $\overline{v_i}(x) := \sum_{s=1}^S v_i(x,t_s)/S$, where $t_s := s\Delta t$. The number of samplings is S. The covariance matrices are represented as $C_{u_i} := \tilde{U}_i \tilde{U}_j^{\mathrm{T}}$ and $C_{v_i} := \tilde{V}_i \tilde{V}_i^{\mathrm{T}}$, where the (m,s) entries of matrices \tilde{U}_i and \tilde{V}_i are $(\tilde{U}_i)_{m,s} = u_i(x_m,t_s) - \overline{u_i}(x_m)$ and $(\tilde{V}_i)_{m,s} = v_i(x_m,t_s) - \overline{v_i}(x_m)$, respectively. The eigenvectors obtained from C_{u_i} and C_{v_i} serve as the basis functions $\Phi^k_{u_i}$ and $\Phi^k_{v_i}$, respectively, normalized to have unit norm, i.e., $\int_0^L (\Phi^k_{u_i}(x))^2 dx = 1$ and $\int_0^L (\Phi^k_{v_i}(x))^2 dx = 1$. The index $k = 1, 2, \ldots, K$ is ordered in descending sequence of the eigenvalues

To begin, we calculate the phase of spatiotemporal dynamics. Figure 6(a) shows the amplitudes of $Q_{u_i}^k$ and $Q_{v_i}^k$, revealing that many of these amplitudes are not nearly zero. Therefore, fluctuations in the corresponding u_i^k and v_i^k influence the correction term. We applied the Poincaré section to either time series of $u_i^{k_p}$ or $v_i^{k_p}$ ($k_p=1$) to calculate $\theta_i^{k_p}$ as shown in Fig. 6(b). The histograms of $\theta_1^{k_p}(t)-\theta_2^{k_p}$ for $n_p=u$ and $n_p=v$ shown in Fig. 6(c) slightly differ from the distribution of $\phi_1-\phi_2$ calculated from the phase equations. The statistics of the correction terms are shown in Fig. 6(d). It indicates

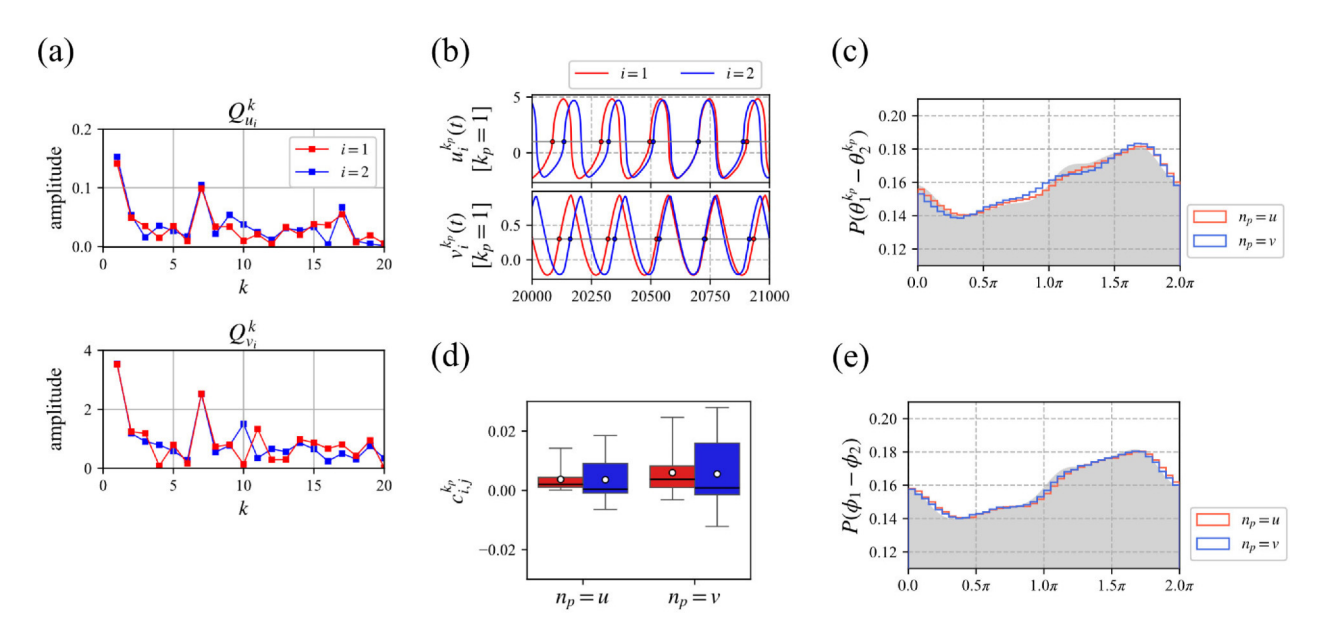


FIG. 6. Calculation of the phase from measurements on all spatial grid points with the decomposition scheme described in Sec. V D. We adopt $k_p=1$. (a) Amplitude of $Q_{u_i}^k$ (top) and $Q_{v_i}^k$ (bottom). The amplitude of $Q_{u_i}^k$ is calculated by $\int_0^{2\pi} |Q_{u_i}^k(\psi)| \mathrm{d}\psi/2\pi$ (a similar formula is used for $Q_{v_i}^k$). The red and blue lines indicate i=1 and i=2, respectively. (b) Time series of $u_i^{k_p}(t)$ (top) and $v_i^{k_p}(t)$ (bottom) and the Poincaré sections. The red and blue lines indicate i=1 and i=2, respectively. The horizontal lines represent the Poincaré sections, and the dots represent the times when $u_i^{k_p}(t)$ or $v_i^{k_p}(t)$ intersects the Poincaré section from negative to positive. (c) Histograms of $\theta_i^{k_p} - \theta_2^{k_p}$ for $n_p = u$ (red) and $n_p = v$ (blue). The histograms are calculated over a duration in which $|\theta_1^{k_p} - \theta_2^{k_p}|$ increases by 200π . The distribution calculated from the phase equations is displayed in gray. (d) Statistics of the correction term $c_{i,j}^{k_p}$ for both $n_p = u$ and $n_p = v$. The red (i=1) and blue (i=2) boxes represent the first and third quartiles of dataset $\{c_{i,j}^{k_p}\}_j$. The horizontal lines mark the medians, while the dots mark the averages. The whiskers extend to show the maximum and minimum values. (e) Histograms of $\phi_1 - \phi_2$ for $n_p = u$ (red) and $n_p = v$ (blue). The histograms are calculated over a duration in which $|\phi_1 - \phi_2|$ increases by 200π . The distribution calculated from the phase equations is displayed in gray.

that the magnitudes of the correction term for both $n_p = u$ and $n_p = v$ are much smaller compared to those calculated from $u_i(x_p, t)$ for $x_p \simeq 15, 30$ [Fig. 4(b)]. Although the magnitude of the correction term for $n_p = u$ is smaller compared to that for $n_p = v$, the difference between them is not a primary concern in this study. To confirm the correction term certainly represents the difference between $\theta_i^{k_p}(t_{i,j}^{k_p})$ and $\phi_i(t_{i,j}^{k_p})$ correctly, we calculated the histogram of $\phi_1 - \phi_2$ on the basis of Eqs. (12) and (13). Figure 6(e) indicates that both histograms of $\phi_1 - \phi_2$ are more similar to the distribution calculated from the phase equations than the histograms of $\theta_1^{k_p} - \theta_2^{k_p}$ shown in Fig. 6(c). These results support the validity of the correction terms. Furthermore, Figs. 10(a) and 10(b) in Appendix E show the phase equations estimated from the time series of $\theta_i^{k_p}$ and ϕ_i , respectively. The phase equations estimated from the time series of $\theta_i^{k_p}$ resemble the true forms qualitatively, while those estimated from the time series of ϕ_i appear to match the true forms even more closely. In Appendix G, we also implement the same scheme for oscillating spots.

E. Case of using the basis function obtained from the phase sensitivity function

According to Eqs. (8) and (12), the correction term can vary depending on the choice of basis functions. The equations indicate that fluctuations in u_i^k and v_i^k do not influence the correction term when their corresponding $Q_{u_i}^k$ and $Q_{v_i}^k$ values

are nearly zero. Therefore, the magnitude of the correction term is expected to be small if the amplitudes of $Q_{u_i}^k$ and $Q_{v_i}^k$ are localized to just a few components. To achieve this localization, we propose using basis functions obtained by applying PCA to the phase sensitivity function, rather than the spatiotemporal dynamics.

We assume that the basis functions, $\Phi_{u_i}^k$ and $\Phi_{v_i}^k$, are derived by solving eigenproblems for the covariance matrices of the phase sensitivity functions $Q_{u_i}(x,\phi_i)$ and $Q_{v_i}(x,\phi_i)$, respectively. The means of phase sensitivity functions over 2π are defined as $\overline{Q_{u_i}}(x) := \sum_{s=1}^S Q_{u_i}(x,\phi_s)/S$ and $\overline{Q_{v_i}}(x) := \sum_{s=1}^S Q_{v_i}(x,\phi_s)/S$, where $\phi_s := \frac{2\pi}{s}s$. The number of uniformly spaced grid points on $[0,2\pi)$ is S. The covariance matrices are represented as $C_{Q_{u_i}} := \tilde{Q}_{u_i} \tilde{Q}_{u_i}^T$ and $C_{Q_{v_i}} := \tilde{Q}_{v_i} \tilde{Q}_{v_i}^T$, where the (m,s) entries of matrices \tilde{Q}_{u_i} and \tilde{Q}_{v_i} are $(\tilde{Q}_{u_i})_{m,s} = Q_{u_i}(x_m,\phi_s) - \overline{Q}_{u_i}(x_m)$, and $(\tilde{Q}_{v_i})_{m,s} = Q_{v_i}(x_m,\phi_s) - \overline{Q}_{v_i}(x_m)$, respectively. The eigenvectors obtained from $C_{Q_{u_i}}$ and $C_{Q_{v_i}}$ serve as the basis functions $\Phi_{u_i}^k$ and $\Phi_{v_i}^k$, respectively, normalized to have unit norm, i.e., $\int_0^L (\Phi_{u_i}^k(x))^2 dx = 1$ and $\int_0^L (\Phi_{v_i}^k(x))^2 dx = 1$. The index $k = 1, 2, \ldots, K$ is ordered in descending sequence of the eigenvalues.

We examine the phase calculation for spatiotemporal dynamics as we do in Sec. V D. Figure 7(a) indicates that the amplitude of $Q_{u_i}^k$ and $Q_{v_i}^k$ are localized to k = 1. In such a situation, the term that contains v_i^1 mainly determines the correction term in the case of $n_p = u$, while the term that

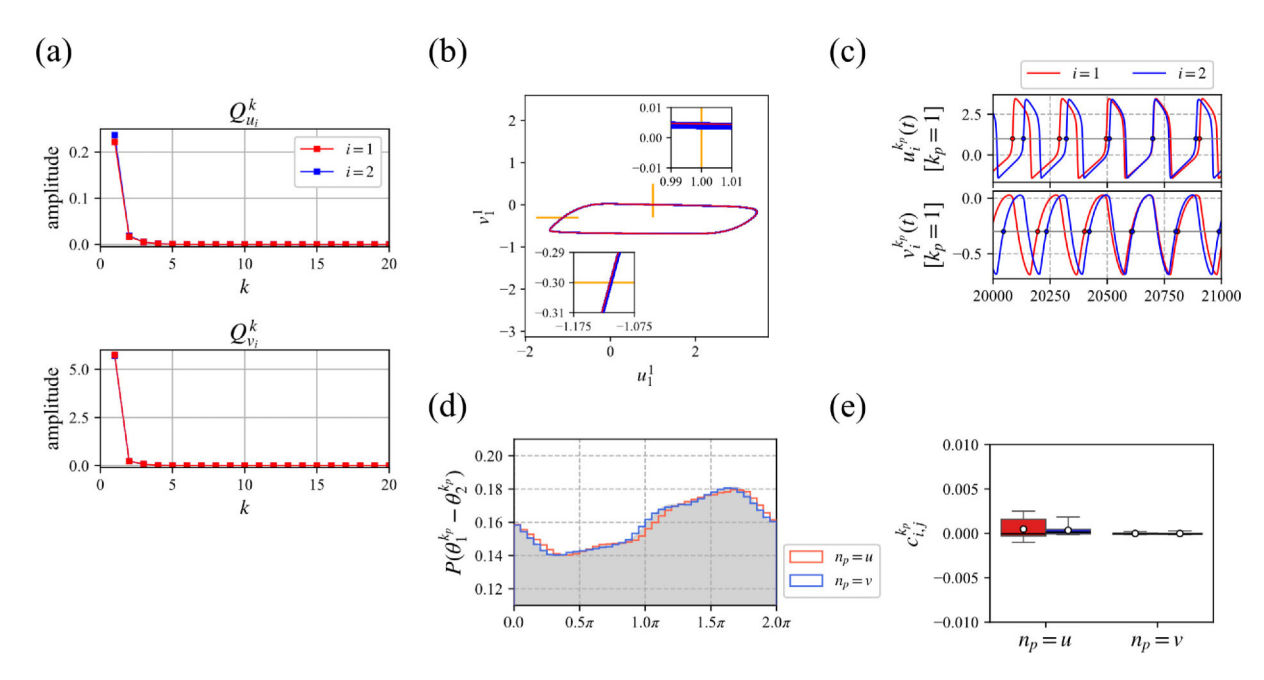


FIG. 7. Calculation of the phase from measurements on all spatial grid points with the decomposition scheme described in Sec. V E. We adopt $k_p=1$. (a) Amplitude of $Q_{u_i}^k$ (top) and $Q_{v_i}^k$ (bottom). The amplitude of $Q_{u_i}^k$ is calculated by $\int_0^{2\pi} |Q_{u_i}^k(\psi)| \mathrm{d}\psi/2\pi$ (a similar formula is used for $Q_{v_i}^k$). The red and blue lines indicate i=1 and i=2, respectively. The amplitudes of $Q_{u_i}^k$ are localized to k=1. (b) Trajectory of (u_1^1, v_1^1) (blue) and the limit-cycle of $(\chi_{u_1}^1, \chi_{v_1}^1)$ (red). The Poincaré sections for $n_p=u$ and $n_p=v$ are depicted with yellow lines, and the insets provide a close-up view around the intersection. (c) Time series of $u_i^{k_p}(t)$ (top) and $v_i^{k_p}(t)$ (bottom) and the Poincaré sections. The red and blue lines represent i=1 and i=2, respectively. The horizontal lines represent the Poincaré sections, and the dots represent the times when $u_i^{k_p}(t)$ or $v_i^{k_p}(t)$ intersects the Poincaré section from negative to positive. (d) Histograms of $\theta_1^{k_p}-\theta_2^{k_p}$ for $n_p=u$ (red) and $n_p=v$ (blue). The histograms are calculated over a duration in which $|\theta_1^{k_p}-\theta_2^{k_p}|$ increases by 200π . The distribution calculated from the phase equations is displayed in gray. (e) Statistics of the correction term $c_{i,j}^{k_p}$ for both $n_p=u$ and $n_p=v$. The red (i=1) and blue (i=2) boxes represent the first and third quartiles of dataset $\{c_{i,j}^{k_p}\}_j$. The horizontal lines mark the medians, while the dots mark the averages. The whiskers extend to show the maximum and minimum values.

contains u_i^1 does the same in the case of $n_p = v$ [Eq. (12)]. This indicates that the magnitude of the correction term is primarily determined by the fluctuations in either u_i^1 or v_i^1 . Since the trajectory of (u_1^1, v_1^1) is close to the limit-cycle of $(\chi_{u_1}^1, \chi_{v_i}^1)$ as shown in Fig. 7(b), the magnitude of the correction terms is expected to be relatively small. We applied the Poincaré section to the time series of $u_i^{k_p}$ or $v_i^{k_p}$ $(k_p = 1)$ to calculate $\theta_i^{k_p}$ [Fig. 7(c)]. The histograms of $\theta_1^{k_p} - \theta_2^{k_p}$ shown in Fig. 7(d) slightly differ from the distribution of $\phi_1 - \phi_2$ calculated from the phase equations. Furthermore, according to the statistics of the correction term shown in Fig. 7(e), its magnitude is much smaller compared to those shown in Fig. 6(d) for both $n_p = u$ and $n_p = v$. These results indicate that using the basis functions obtained by applying PCA to the phase sensitivity function reduces the magnitude of the correction term. Since the correction term is nearly negligible, ignoring it does not substantially degrade the accuracy of phase equation estimation. Figure 11 in Appendix E shows that the phase equations estimated from the time series of $\theta_{\cdot}^{k_p}$ closely resemble the true forms.

As previously discussed, the localization of the amplitudes of $Q_{u_i}^k$ and $Q_{v_i}^k$ is an important factor to reduce the magnitude of the correction terms. According to Eq. (12), when $Q_{u_i}^k$ and $Q_{v_i}^k$ have large amplitudes, fluctuations in u_i^k and v_i^k significantly influence the correction term. Thus, the degree

of localization is related to the extent to which the correction term can be reduced. For target waves, where the phase sensitivity function possesses a rigid coherent structure [see Fig. 8(b) in Appendix C], $Q_{u_i}^1$ and $Q_{v_i}^1$ predominantly capture the phase sensitivity function. By contrast, in the case of oscillating spots where the phase sensitivity function exhibits the deformation of a coherent structure, several $Q_{u_i}^k$ and $Q_{v_i}^k$ are necessary to approximate it (Appendix G). In summary, the PCA-based scheme mentioned here is effective for target waves since only the fluctuation of either u_i^1 or v_i^1 impacts the correction term although this scheme is less effective for oscillating spots, where the fluctuations of several u_i^k and v_i^k influence the correction term. Furthermore, the magnitude of these fluctuations plays a crucial role in determining the magnitude of the correction term. For example, given that Q_{μ}^{1} and $Q_{v_i}^1$ have the largest amplitude, the fluctuation in either u_i^1 or v_i^1 remains a significant contributor to the correction term [see Eq. (12)].

VI. DISCUSSION

The investigations in this paper are summarized as follows. First, we briefly reviewed the phase reduction theory for PDE to introduce the concept of phase (Sec. II). We utilized weakly coupled FHN reaction-diffusion models exhibiting target waves in a numerical simulation (Sec. III)

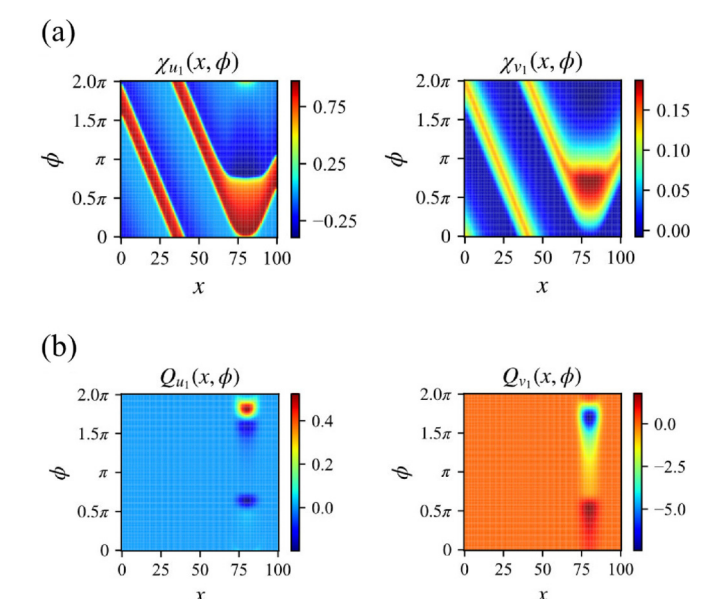


FIG. 8. Limit-cycle solutions and phase sensitivity functions for the FHN reaction-diffusion model described in Sec. III (a) Limit cycle of the target-wave solution $\chi_1(x,\phi) = (\chi_{u_1}(x,\phi), \chi_{v_1}(x,\phi))$. (b) Phase sensitivity function of the target-wave solution $Q_1(x,\phi) = (Q_{u_1}(x,\phi), Q_{v_1}(x,\phi))$.

to illustrate the phase calculation. We examined the methods for calculating phase based on measurements taken at a single spatial grid point (Sec. IV) and those taken across all spatial grid points (Sec. V). Additionally, we applied the phase calculation methods described in Secs. IV and V to spatiotemporal dynamics with oscillating spots (Appendix G). In Sec. IV and Appendix G, we observed that the magnitude of the correction term is small when the Poincaré section is applied to measurement time series from a single grid point within either the pacemaker region, which emits target waves, or the spot's front region. These regions are known to possess phase sensitivity functions with large amplitudes. While the phase sensitivity functions for real-world systems are generally unknown, it is likely that they are localized in regions that govern overall dynamics [56]. Therefore, identifying optimal measurement positions based on experimental and theoretical insights is advisable, as these regions may visibly control the rhythms of spatiotemporal dynamics. In Sec. V and Appendix G, we proposed a scheme aimed at localizing the amplitude of the (decomposed) phase sensitivity function to a few key components (Sec. VE). Our results for target waves and oscillating spots indicate that the scheme's effectiveness depends on whether the phase sensitivity function possesses a coherent structure without or with deformation. Notably, phase calculations for target waves can achieve a reasonable accuracy even without this PCA scheme (Sec. VD).

Properly setting the Poincaré section is crucial not only for continuous systems but also for real-world discrete systems, including the network of dynamical elements exhibiting the collective oscillation [49,52,79]. This necessity arises because a large magnitude of the correction term can also occur in high-dimensional ODE systems, especially when the dimension of the dynamical system is comparable to the number of

spatial grid points in PDE cases. This can be explained by the fact that the expressions for the correction terms in the ODE and PDE cases have a similar form [see Eq. (A3) in Appendix A and Eq. (B4) in Appendix B]. Furthermore, although we assumed the one-dimensional space, the approach for setting the Poincaré section discussed in this study is also applicable to multidimensional spaces. This is because the localization of phase sensitivity functions for rhythmic patterns occurs similarly in multidimensional spaces [56].

The findings of this study provide insights for calculating the phase from measurements across various domains such as meteorology [80,81], electrochemical oscillators [82], biophysics [83], and life science [84]. When measuring at a single grid point, the accuracy of phase calculation is improved by taking measurements from the pacemaker region or the region where the front of the oscillating spot exists. In addition, for systems exhibiting target waves, it is possible to calculate the phase from a one-dimensional time series obtained by applying PCA to multidimensional measurements over multiple spatial grid points. For example, in meteorology, PCA (also known as empirical orthogonal functions) is sometimes applied to spatiotemporal dynamics to obtain the time series of modes (and its basis function). Our study suggests that these modes can sometimes be used to calculate the phase. The findings of this study can be experimentally verified using a pair of photosensitive Belousov-Zhabotinsky systems, where two spatiotemporal rhythmic patterns are locally coupled via video cameras and projectors [85].

Our key finding allows for the calculation of the phase of collective oscillations of dynamical elements [49,52,79] and spatiotemporal dynamics [56] from measurements. Therefore, the phase response, phase sensitivity function, and phase coupling function of the collective oscillation and spatiotemporal dynamics can be estimated by combining our method with conventional estimation methods [8-23] as we did in Appendix E. To ensure accurate estimation, it is crucial to reduce the magnitude of the correction term caused by the discrepancy between the Poincaré section and the isochron. This study revealed a proper setting for the Poincaré section that realizes the calculation of the phase with a small magnitude of the correction term. The setting is based on the spatial localization of the phase sensitivity function. Ignoring these considerations can lead to incorrect estimations and misunderstandings of system properties, as shown by the incorrectly estimated phase equations (see Appendix E for target waves and Appendix G for oscillating spots).

This study showed that even in the absence of noise, a difference exists between the calculated phase and the isochron-based phase, and we investigated methods to reduce this difference. Addressing the robustness of phase calculation under the noise remains a future task. Furthermore, in this study, we assumed that the basis functions for the orthogonal decomposition were obtained using PCA. Other techniques, such as extended dynamic mode decomposition (EDMD) [86,87], which identifies non-self-adjoint left and right vectors from multidimensional measurements, could also be used for orthogonal decomposition. Developing a method that utilizes EDMD is a future challenge and might enable the calculation of the phase for spatiotemporal dynamics exhibiting oscillating spots with a smaller magnitude of the correction term.

Finally, some spatiotemporal dynamics have multiple phases, e.g., the governing equation has a limit-torus solution [88]. Future research should also address the phase calculation for the systems exhibiting multiple rhythms.

ACKNOWLEDGMENTS

This work was supported by JSPS (Japan) KAKENHI Grants No. JP24K23908, No. JP24K06910, No. JP24H00723, No. JP20K03797, and No. JP20K20520; MEXT KAKENHI Grant No. JP23H04467. Numerical simulations were conducted using Earth Simulator at JAMSTEC.

APPENDIX A: CALCULATION OF THE ISOCHRON-BASED PHASE BY LINEAR APPROXIMATION IN THE VICINITY OF LIMIT-CYCLE SOLUTION OF ODE

Let us consider the following ODE:

$$\dot{X}(t) = F(X),\tag{A1}$$

where $X \in \mathbb{R}^N$ represents the state variable. We assume that Eq. (A1) has a limit-cycle solution χ with period T. According to phase reduction theory [1,2], the multidimensional state space is mapped to a one-dimensional space characterized by a periodic variable, $\phi \in [0, 2\pi)$, called phase. Here, let us consider a state, $X_0(t)$, which evolves along the limit-cycle solution. The phase $\phi(t)$ is assigned to $X_0(t)$ such that it increases linearly with a constant frequency $\omega := 2\pi/T$ as time progresses, i.e., $\phi(t) = \omega t$. We define the state on the limit-cycle solution as $\chi(\phi(t)) := X_0(t)$. Next, we extend the definition of the phase to the basin of attraction. We assign the same phase value to a subset of the state space defined as follows:

$$I(\psi) = \{X(t) \Big| \lim_{t \to +\infty} \|X(t) - \chi(\phi(t))\| = 0, \ \phi(0) = \psi \},$$
(A2)

where $\|\cdot\|$ denotes the L^2 norm defined as $\|A\| = \sqrt{A \cdot A}$. The subset assigned phase value ϕ is represented as $I(\phi)$. By analyzing the isochrons corresponding to each phase value, we can determine a scalar field that represents the configuration of the phase over the basin of attraction. The time series of the phase $\phi(t)$ is obtained by assigning the phase value to the time series of X(t) on the basis of this scalar field.

The concept of the isochron provides a linear approximation in the vicinity of the limit-cycle solution. We consider a state X', which is slightly kicked out from the state $\chi(\psi_0)$ by a weak perturbation. The phase ψ assigned to X' is calculated as follows:

$$\psi = \psi_0 + \mathbf{Z}(\psi_0) \cdot (\mathbf{X}' - \mathbf{\chi}(\psi_0))$$

$$= \psi_0 + \sum_{n=1}^{N} Z_n(\psi_0) (X'_n - \chi_n(\psi_0)), \tag{A3}$$

where $\mathbf{Z}(\psi_0) \in \mathbb{R}^N$ is the phase sensitivity function, which quantifies linear response characteristics of the phase to weak perturbation, and the subscript n denotes the nth entry of the vector. When the two states, \mathbf{X}' and $\mathbf{\chi}(\psi_0)$, lie on the same Poincaré section that defines $\psi_0 = 0$, the second term can be

considered as a correction term, and ψ is interpreted as the isochron-based phase.

APPENDIX B: CALCULATION OF THE ISOCHRON-BASED PHASE BY LINEAR APPROXIMATION IN THE VICINITY OF LIMIT-CYCLE SOLUTION OF PDE

Similar to the ODE described in Appendix A, the concept of isochron can be applied to the PDE [56]. Let us consider the equation described in Eq. (1) without the coupling (G = 0) as follows (the subscript i is removed for convenience):

$$\frac{\partial}{\partial t}X(\mathbf{r},t) = \mathbf{F}(X,\mathbf{r}) + D\nabla^2 X. \tag{B1}$$

We assume that Eq. (B1) has a limit-cycle solution χ with period T. According to the phase reduction theory extended to the PDE [56], the infinite-dimensional state space is mapped to a one-dimensional space characterized by a periodic variable, $\phi \in [0, 2\pi)$. Here, let us consider a state, $X_0(r, t)$, which evolves along the limit-cycle solution. The phase $\phi(t)$ is assigned on $X_0(r,t)$ such that it increases linearly with constant frequency $\omega := 2\pi/T$ as time progresses, i.e., $\phi(t) = \omega t$. We define a state on the limit-cycle solution as $\chi(r,\phi(t)) := X_0(r,t)$. Next, we extend the definition of the phase to the basin of attraction. We assign the same phase value to a subset of the state space as follows:

$$I(\psi) = \left\{ X(\mathbf{r}, t) \middle| \lim_{t \to +\infty} ||X(\mathbf{r}, t) - \chi(\mathbf{r}, \phi(t))|| = 0, \ \phi(0) = \psi \right\},$$
(B2)

where $\|\cdot\|$ denotes the L^2 norm defined as $\|A(r)\| = \sqrt{\int A(r) \cdot A(r) \mathrm{d}r}$. We denote the subset assigned phase value ϕ as $I(\phi)$. By analyzing the isochrons corresponding to each phase value, we can determine a scalar field that represents the configuration of the phase over the basin of attraction. Therefore, the time series of the phase $\phi(t)$ is obtained by assigning the phase value to the time series of X(r,t) on the basis of this scalar field.

The concept of the isochron provides a linear approximation in the vicinity of the limit-cycle solution. We consider a state X'(r), which is slightly kicked out from a state $\chi(r, \psi_0)$ by a weak perturbation. The phase ψ assigned to X' is calculated as follows:

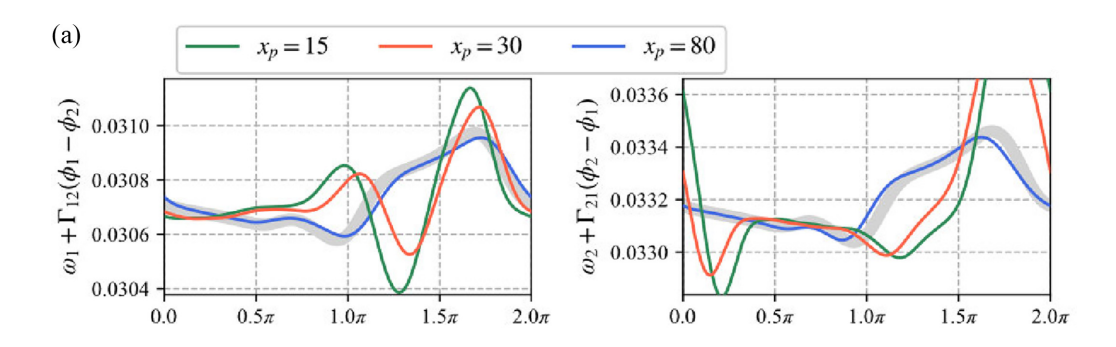
$$\psi = \psi_0 + \int \mathbf{Q}(\mathbf{r}, \psi_0) \cdot (\mathbf{X}'(\mathbf{r}) - \mathbf{\chi}(\mathbf{r}, \psi_0)) d\mathbf{r}$$

$$= \psi_0 + \int \sum_{n=1}^N \mathbf{Q}_n(\mathbf{r}, \psi_0) (X'_n(\mathbf{r}) - \mathbf{\chi}_n(\mathbf{r}, \psi_0)) d\mathbf{r}, \quad (B3)$$

where Q is the phase sensitivity function and the subscript n denotes the nth entry of the vector. For simplicity, we assume a one-dimensional space, i.e., $r \to x$. Given the spatial grid, $x_m = m\Delta x \, (m = 0, 1, \ldots, M)$, Eq. (B3) is rewritten with discrete representation as follows:

$$\psi = \psi_0 + \sum_{m=0}^{M} \sum_{n=1}^{N} Q_n(x_m, \psi_0) (X'_n(x_m) - \chi_n(x_m, \psi_0)) \Delta x_m,$$

$$\Delta x_m := \begin{cases} \Delta x/2 & (m = 0, M), \\ \Delta x & (\text{otherwise}). \end{cases}$$
 (B4)



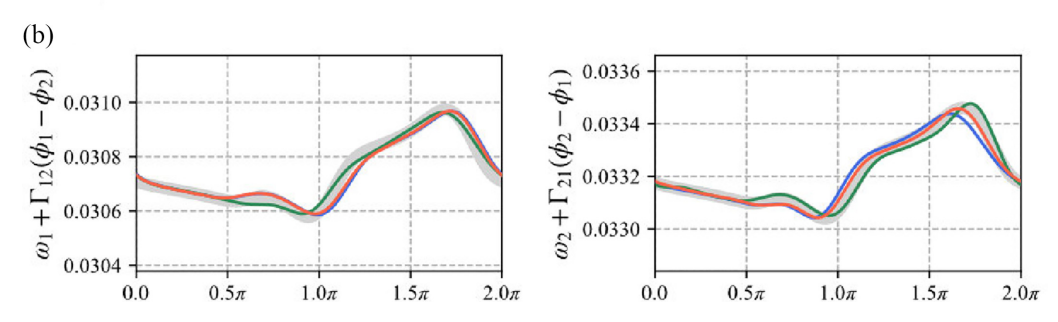


FIG. 9. Phase equations estimated from the time series of the phase calculated from measurements taken at a single spatial grid point (see Sec. IV C). The colored lines display the phase equations estimated from the time series of $\theta_i^{x_p}(t)$ or $\phi_i(t)$. The legend denotes the correspondence between the colors of the lines and the values of x_p . The true forms of the phase equations are displayed in bold-gray lines. (a) Results obtained from $\theta_i^{x_p}$. (b) Results obtained from ϕ_i .

The calculation of the correction term in Eq. (4) is derived from this equation. When we replace the variables in Eq. (B4) with $\psi \to 2\pi j + c_{i,j}^{x_p}$, $\psi_0 \to 2\pi j$, $Q_n(x_m, \psi_0) \to Q_{i,n}(x_m, 0)$, $X'_n(x_m) \to X_{i,n}(x_m, t_{i,j}^{x_p})$, and $\chi_n(x_m, \psi_0) \to \chi_{i,n}(x_m, 0)$ and then consider $X_{i,n_p}(x_{m_p}, t_{i,j}^{x_p}) - \chi_{i,n_p}(x_{m_p}, 0) = 0$, we obtain Eq. (4).

APPENDIX C: LIMIT-CYCLE SOLUTION AND PHASE SENSITIVITY FUNCTION OF THE FHN REACTION-DIFFUSION MODEL

The FHN reaction-diffusion model described in Sec. III has the limit-cycle solution $\chi_i(x, \phi_i) = (\chi_{u_i}(x, \phi_i), \chi_{v_i}(x, \phi_i))$ and the phase sensitivity function $Q_i(x, \phi_i) = (Q_{u_i}(x, \phi_i), Q_{v_i}(x, \phi_i))$. The limit-cycle solution χ_1 and the phase sensitivity function Q_1 for the target-wave solution are shown in Figs. 8(a) and 8(b).

APPENDIX D: PHASE EQUATIONS OF THE FHN REACTION-DIFFUSION MODEL

Phase reduction theory extended to the PDE [56] allows for deriving a phase equation from a PDE with a limit-cycle solution. The FHN reaction-diffusion model falls within the applicability of this theory. For a pair of weakly coupled reaction-diffusion models described by Eq. (1), the phase equations are given by

$$\dot{\phi}_1(t) = \omega_1 + \Gamma_{12}(\phi_1 - \phi_2),
\dot{\phi}_2(t) = \omega_2 + \Gamma_{21}(\phi_2 - \phi_1),$$
(D1)

where $\omega_i := 2\pi/T_i$ represents the frequency of the limit-cycle solution χ_i of Eq. (1) without coupling (G = 0). The constant T_i represents the period of the limit-cycle solution. The phase coupling functions between the two phases, Γ_{12} and Γ_{21} , describe how the phases are affected by the coupling function G. The phase equations for the coupled FHN reaction-diffusion models that simulate target waves are displayed in Fig. 9 in Appendix E. (Figures 10 and 11 in Appendix E also show the same.)

The distribution of $\phi_1 - \phi_2$ shown in several figures was calculated using the phase equations [see the gray plots in Figs. 2(c), 4(c), 6(c), 6(e), and 7(d)]. This distribution is inversely related to the velocity of $\phi_1 - \phi_2$. We calculated it by taking the reciprocal of the difference between the phase equations, i.e., $P(\phi_1 - \phi_2) \propto 1/(\omega_1 - \omega_2 + \Gamma_{12}(\phi_1 - \phi_2) - \Gamma_{21}(-[\phi_1 - \phi_2]))$. Additionally, Appendix G presents the phase equations and distribution of $\phi_1 - \phi_2$ derived from the model simulating oscillating spots.

APPENDIX E: ESTIMATING THE PHASE EQUATIONS

Neglecting the correction term during phase calculation introduces errors in estimating the phase equations [Eq. (D1)], with the error becoming more significant as the magnitude of the correction term increases. To illustrate this, we estimated the phase equations using the approach from Ref. [22].

Figures 9(a) and 9(b) show the phase equations estimated from the time series of $\theta_i^{x_p}(t)$ and $\phi_i(t)$, respectively, for spatiotemporal dynamics featuring target waves (Sec. III). Examining the results for $x_p \simeq 15,30$ shown in Fig. 9(a),

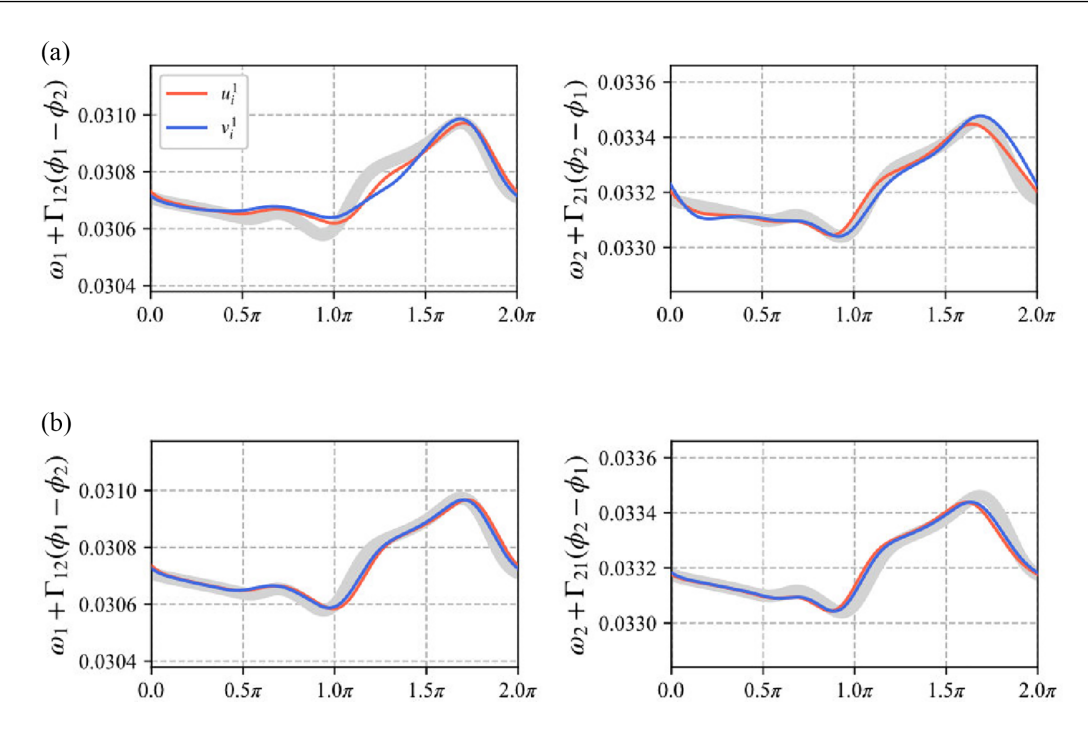


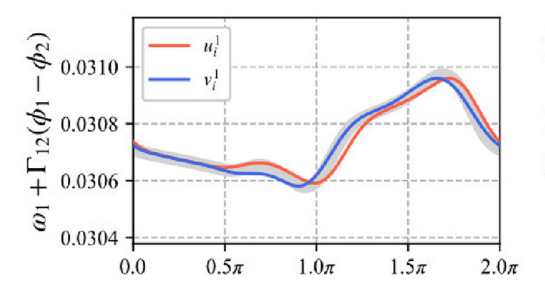
FIG. 10. Phase equations estimated from the time series of the phase calculated from measurements taken at all spatial grid points. The orthogonal decomposition scheme described in Sec. V D is used. The red and blue lines display the phase equations obtained from the time series of $u_i^{k_p}(t)$ and $v_i^{k_p}(t)$ ($k_p = 1$), respectively. The true forms of the phase equations are displayed in bold gray lines. (a) Results obtained from $\theta_i^{k_p}$. (b) Results obtained from ϕ_i .

we see that a large magnitude of the correction term [see Fig. 4(b)] leads to significant discrepancies between the estimated phase equations and the true forms, indicated by bold-gray lines. In contrast, for $x_p \simeq 80$, where the correction term is small, the estimated phase equations closely align with the true forms. These findings indicate that omitting the correction term impacts the estimation accuracy, with the extent of impact linked to the magnitude of the correction term. In addition, all phase equations estimated from the time series of $\phi_i(t)$ closely resemble the true forms [Fig. 9(b)]. This suggests that incorporating correction terms in phase calculation effectively reduces estimation errors in the phase equations.

Similar estimations are presented in Sec. VD. Figures 10(a) and 10(b) show phase equations estimated from time series of $\theta_i^{k_p}(t)$ and $\phi_i(t)$, respectively (we consider $k_p =$

1). The results in Fig. 10(a) show close alignment with the true forms owing to the small magnitude of the correction terms, which reduces errors in the estimation of the phase equation. The phase equations estimated from the time series of $\phi_i(t)$ shown in Fig. 10(b) are more accurate than those estimated from the time series of $\theta_i^{k_p}(t)$.

Section VE repeats estimations of the same phase equations, with Fig. 11 presenting phase equations estimated from the time series of $\theta_i^{k_p}(t)$ for spatiotemporal dynamics. Figures 10(a) and 11 both show phase equations estimated from $\theta_i^{k_p}(t)$ for target waves, using different decomposition schemes (see Secs. VD and VE). The latter estimation captures more detailed phase equation features than the former, indicating that the scheme in Sec. VE reduces the magnitude of the correction term and improves the estimation of the phase equations.



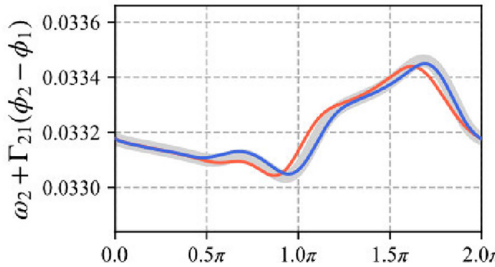


FIG. 11. Phase equations estimated from the time series of the phase calculated from measurements taken at all spatial grid points. The orthogonal decomposition scheme described in Sec. VE is used. The red and blue lines display the phase equations obtained from the time series of $u_i^{k_p}(t)$ and $v_i^{k_p}(t)$ ($k_p = 1$), respectively. The true forms of the phase equations are displayed in bold-gray lines.

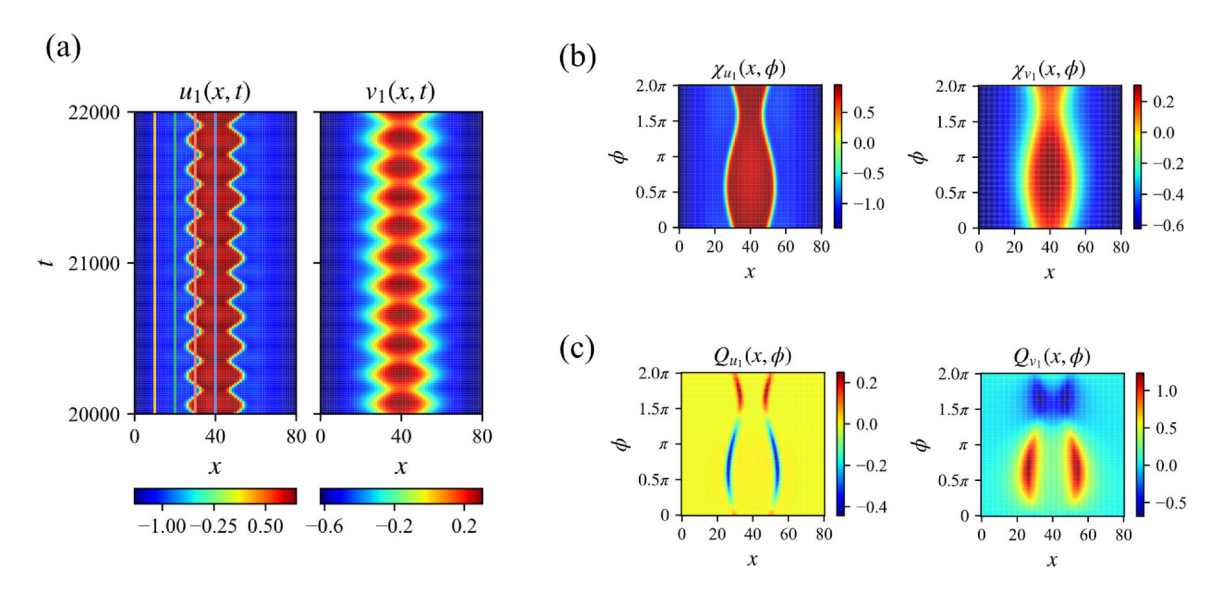


FIG. 12. Illustration of FHN reaction-diffusion models used in Appendix G. (a) Spatiotemporal dynamics of oscillating spots simulated by the coupled FHN reaction-diffusion models. For reference, the yellow, green, red, and blue vertical lines mark the measurement positions, $x_p = 10, 20, 30, 40$, respectively. (b) Limit cycle of the oscillating spot solution $\chi_1(x, \phi)$. (c) Phase sensitivity function of the oscillating spot solution $Q_1(x, \phi)$.

The detailed estimation method is found in Ref. [22]. Hyperparameters are set as $\chi_i^{\text{old}} = (\bar{\omega}_i, 0, 0, \dots, 0)^T$, $\Sigma_i^{\text{old}} = \lambda_i^{-1}E$, and $\alpha_i^{\text{old}} = \beta_i^{\text{old}} = 0.001$ (see Ref. [22]), where $\bar{\omega}_i$ is the mean velocity calculated from the time series of the phase, and E denotes an identity matrix. In addition, to optimize the marginal likelihood functions, we set λ_i , which represents the magnitude of Σ_i^{old} , and M_i , which represents the Fourier series order in the phase coupling function. (These parameters were determined in the range of $M_i = 0, 1, \dots, 10$ and $\log_{10} \lambda_i = 1, 2, \dots, 5$.) Phase equations were estimated from phase time series during intervals where $|\phi_1 - \phi_2|$ increases by 200π .

APPENDIX F: THE ORTHOGONALLY DECOMPOSED PHASE SENSITIVITY FUNCTION

We mention the derivation of Eq. (11). Let us consider the state variable $X(x, t) \in \mathbb{R}^N$, which obeys

$$\frac{\partial}{\partial t} X(x,t) = F(X,x) + \epsilon p(x,t), \tag{F1}$$

where F(X,x) represents the local dynamics at point x and time t, p(x,t) represents the local perturbation to X(x,t), and $\epsilon \ll 1$ represents the intensity of the perturbation. For simplicity, the local dynamics F includes any diffusion of X if present. We assume that Eq. (F1), in the absence of coupling (p=0), has a limit-cycle solution $\chi(x,\phi)$ with $\phi=[0,2\pi)$. Additionally, we assume that the perturbation is sufficiently weak so that X does not deviate significantly from the limit-cycle solution. Given the phase sensitivity function $Q(x,\phi)$ for the limit-cycle solution, the phase equation is derived as follows [56]:

$$\dot{\phi}(t) = \omega + \epsilon \int_0^L \mathbf{Q}(x, \phi) \cdot \mathbf{p}(x, t) dx$$

$$= \omega + \epsilon \int_0^L \sum_{n=1}^N \mathbf{Q}_n(x, \phi) p_n(x, t) dx, \qquad (F2)$$

where, subscript n denotes the nth entry of the vectors, L is the size of the system, and ω is frequency of the limit-cycle solution.

We consider mapping from an infinite-dimensional state space to the KN-dimensional space through orthogonal decomposition. Given a set of orthonormal basis functions $\Phi_n^k (n=1,2,\ldots,N,\ k=1,2,\ldots,K)$, the N-dimensional state or functions, $\tilde{\boldsymbol{X}}^k(t)=(\tilde{X}_1^k(t),\tilde{X}_2^k(t),\ldots,\tilde{X}_N^k(t))$, $\tilde{\boldsymbol{Q}}^k(\phi)=(\tilde{Q}_1^k(\phi),\tilde{Q}_2^k(\phi),\ldots,\tilde{Q}_N^k(\phi))$, $\tilde{\boldsymbol{F}}^k(\boldsymbol{X})=(\tilde{F}_1^k(\boldsymbol{X}),\tilde{F}_2^k(\boldsymbol{X}),\ldots,\tilde{F}_N^k(\boldsymbol{X}))$, and $\tilde{\boldsymbol{p}}^k(t)=(\tilde{p}_1^k(t),\tilde{p}_2^k(t),\ldots,\tilde{p}_N^k(t))$ are obtained as follows:

$$\tilde{X}_n^k(t) = \int_0^L X_n(x, t) \Phi_n^k(x) dx,$$

$$\tilde{Q}_n^k(\phi) = \int_0^L Q_n(x, \phi) \Phi_n^k(x) dx,$$

$$\tilde{F}_n^k(X) = \int_0^L F_n(X, x) \Phi_n^k(x) dx,$$

$$\tilde{p}_n^k(t) = \int_0^L p_n(x, t) \Phi_n^k(x) dx,$$
(F3)

where the basis function satisfies $\int_0^L \Phi_n^p(x) \Phi_n^q(x) = \delta_{pq}$. The tilde indicates that the value is obtained by projection onto the basis functions. We assume that the number of the component K is sufficiently large to ensure that each function can be reproduced nearly 100%. The dynamics of the state variable X_n^k projected onto $\Phi_n^k(x)$ obeys

$$\frac{\partial}{\partial t}\tilde{X}_{n}^{k}(t) = \tilde{F}_{n}^{k}(X) + \epsilon \tilde{p}_{n}^{k}(t). \tag{F4}$$

We rewrite Eq. (F4) with *N*-dimensional vector representation as follows:

$$\frac{\partial}{\partial t}\tilde{\boldsymbol{X}}^{k}(t) = \tilde{\boldsymbol{F}}^{k}(\boldsymbol{X}) + \epsilon \tilde{\boldsymbol{p}}^{k}(t). \tag{F5}$$

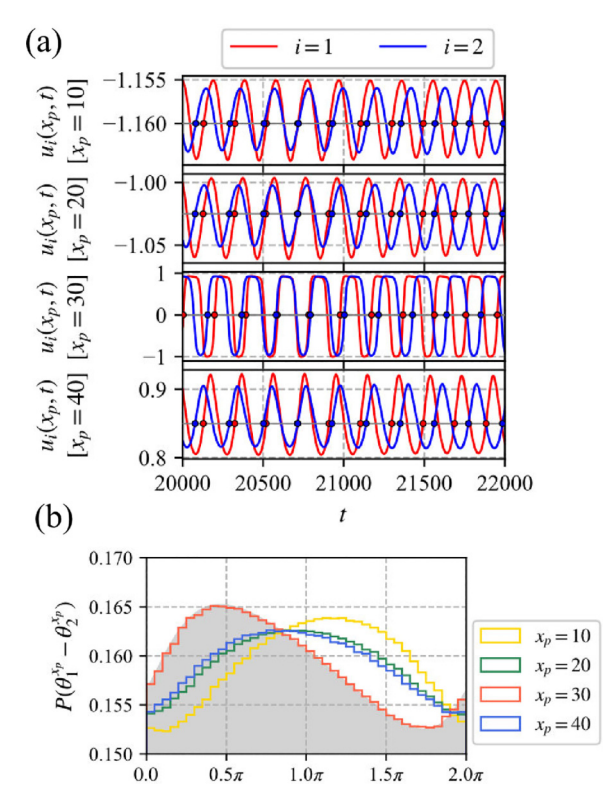


FIG. 13. Time series of $u_i(x_p,t)$ and the calculation of $\theta_i^{x_p}(t)$ for the spatiotemporal dynamics exhibiting oscillating spots (Appendix G). (a) Time series of $u_i(x_p,t)$ and the Poincaré sections for $x_p=10,20,30,40$. The red and blue lines indicate i=1 and i=2, respectively. The horizontal lines depict the Poincaré sections, while the dots represent the times at which $u_i(x_p,t)$ intersects the Poincaré section from negative to positive. (b) Histograms of $\theta_1^{x_p} - \theta_2^{x_p}$ for $x_p=10$ (yellow), 20 (green), 30 (red), and 40 (blue). The histograms are calculated over a duration in which $|\theta_1^{x_p} - \theta_2^{x_p}|$ increases by 200π . The distribution calculated from the phase equations is displayed in gray.

Given Eq. (F5) for k = 1, 2, ..., K, the state variable $\tilde{X}(t) = (\tilde{X}^1(t), \tilde{X}^2(t), ..., \tilde{X}^K(t)) \in \mathbb{R}^{KN}$ is subjected to the perturbation $\tilde{p}(t) = (\tilde{p}^1(t), \tilde{p}^2(t), ..., \tilde{p}^K(t)) \in \mathbb{R}^{KN}$. The limit-cycle solution of Eq. (F1) persists as the limit-cycle solution of Eq. (F5), albeit it deformed. Therefore, there exists a phase equation that describes the phase response to the perturbation \tilde{p} , as follows:

$$\dot{\boldsymbol{\phi}}(t) = \omega + \epsilon \hat{\boldsymbol{Q}}(\boldsymbol{\phi}) \cdot \tilde{\boldsymbol{p}}(t)$$

$$= \omega + \epsilon \sum_{k=1}^{K} \hat{\boldsymbol{Q}}^{k}(\boldsymbol{\phi}) \cdot \tilde{\boldsymbol{p}}^{k}(t)$$

$$= \omega + \epsilon \sum_{k=1}^{K} \sum_{n=1}^{N} \hat{\boldsymbol{Q}}_{n}^{k}(\boldsymbol{\phi}) \tilde{\boldsymbol{p}}_{n}^{k}(t), \tag{F6}$$

where unknown $\hat{\boldsymbol{Q}}(\phi) = (\hat{\boldsymbol{Q}}^1(\phi), \hat{\boldsymbol{Q}}^2(\phi), \dots, \hat{\boldsymbol{Q}}^K(\phi)) \in \mathbb{R}^{KN}$ with $\hat{\boldsymbol{Q}}^k(\phi) = (\hat{Q}_1^k(\phi), \hat{Q}_2^k(\phi), \dots, \hat{Q}_N^k(\phi))$ represents the linear response characteristics of the phase to the perturbation $\tilde{\boldsymbol{p}}$. The frequency ω in Eq. (F6) is the same as that in Eq. (F2) since the period of the limit-cycle solution of Eq. (F1) and Eq. (F5) must have same period.

Here, we derive what the unknown function \hat{Q} is. From Eqs. (F2) and (F6), we obtain the following equation:

$$\int_{0}^{L} \sum_{n=1}^{N} Q_{n}(x,\phi) p_{n}(x,t) dx = \sum_{k=1}^{K} \sum_{n=1}^{N} \hat{Q}_{n}^{k}(\phi) \tilde{p}_{n}^{k}(t).$$
 (F7)

We also obtain the following equation starting from the left-hand side of Eq. (F7):

$$\int_{0}^{L} \sum_{n=1}^{N} Q_{n}(x,\phi) p_{n}(x,t) dx
= \int_{0}^{L} \sum_{n=1}^{N} Q_{n}(x,\phi) \left[\sum_{k=1}^{K} \tilde{p}_{n}^{k}(t) \Phi_{n}^{k}(x) \right] dx
= \sum_{k=1}^{K} \sum_{n=1}^{N} \left[\int_{0}^{L} Q_{n}(x,\phi) \Phi_{n}^{k}(x) dx \right] \tilde{p}_{n}^{k}(t)
= \sum_{k=1}^{K} \sum_{n=1}^{N} \tilde{Q}_{n}^{k}(\phi) \tilde{p}_{n}^{k}(t).$$
(F8)

The transformation to the second and fourth rows is achieved by substituting $p_n(x,t) \simeq \sum_{k=1}^K \tilde{p}_n^k(t) \Phi_n^k(x)$ and $\tilde{Q}_n^k(t) = \int_0^L Q_n(x,t) \Phi_n^k(x) dx$, respectively. Finally, we derived $\hat{Q}_n^k(\phi) = \tilde{Q}_n^k(\phi)$ from Eqs. (F7) and (F8), and thus we obtain the following equation from Eq. (F6):

$$\dot{\phi}(t) = \omega + \epsilon \sum_{k=1}^{K} \sum_{n=1}^{N} \tilde{Q}_{n}^{k}(\phi) \tilde{p}_{n}^{k}(t). \tag{F9}$$

We also obtain the equation with vector representation as follows:

$$\dot{\phi}(t) = \omega + \epsilon \sum_{k=1}^{K} \tilde{\boldsymbol{Q}}^{k}(\phi) \cdot \tilde{\boldsymbol{p}}^{k}(t)$$

$$= \omega + \epsilon \tilde{\boldsymbol{Q}}(\phi) \cdot \tilde{\boldsymbol{p}}(t). \tag{F10}$$

Equations (F9) and (F10) indicate that \tilde{Q} serves as the phase sensitivity function when the infinite-dimensional state space is mapped to the finite-dimensional space spanned by basis functions as described in Eq. (F3).

We denote the limit-cycle solution projected onto the basis functions as $\tilde{\chi}(\phi) \in \mathbb{R}^{KN}$, whose *n*th entry is calculated by $\tilde{\chi}_n^k(t) = \int_0^L \chi_n(x,t) \Phi_n^k(x) dx$. In the previous paragraph, we found that $\tilde{\boldsymbol{Q}}$ represents the linear response characteristics of the phase to the perturbation $\tilde{\boldsymbol{p}}$ when $\tilde{\boldsymbol{Q}}$ and $\tilde{\boldsymbol{p}}$ are obtained by the projection onto the same basis functions. Therefore, the phase ψ assigned to a state $\tilde{\boldsymbol{X}}' \in \mathbb{R}^{KN}$, which is slightly kicked out from the state $\tilde{\boldsymbol{\chi}}(\psi_0)$, is calculated as follows:

$$\psi = \psi_0 + \tilde{\mathbf{Q}}(\psi_0) \cdot (\tilde{\mathbf{X}}' - \tilde{\mathbf{\chi}}(\psi_0))$$

$$= \psi_0 + \sum_{k=1}^K \sum_{n=1}^N \tilde{\mathbf{Q}}_n^k(\psi_0) ([\tilde{\mathbf{X}}']_n^k - \chi_n^k(\psi_0)).$$
 (F11)

The calculation of the correction term in Eq. (11) is based on this equation. Specifically, when we replace the variables in Eq. (F11) with $\psi \to 2\pi j + c_{i,j}^{k_p}$, $\psi_0 \to 2\pi j$, $\tilde{Q}_n^k(\psi_0) \to Q_{i,n}^k(0)$, $[\tilde{X}']_n^k \to X_{i,n}^k(t_{i,j}^k)$, and $\tilde{\chi}_n^k(\psi_0) \to \chi_{i,n}^k(0)$ and then

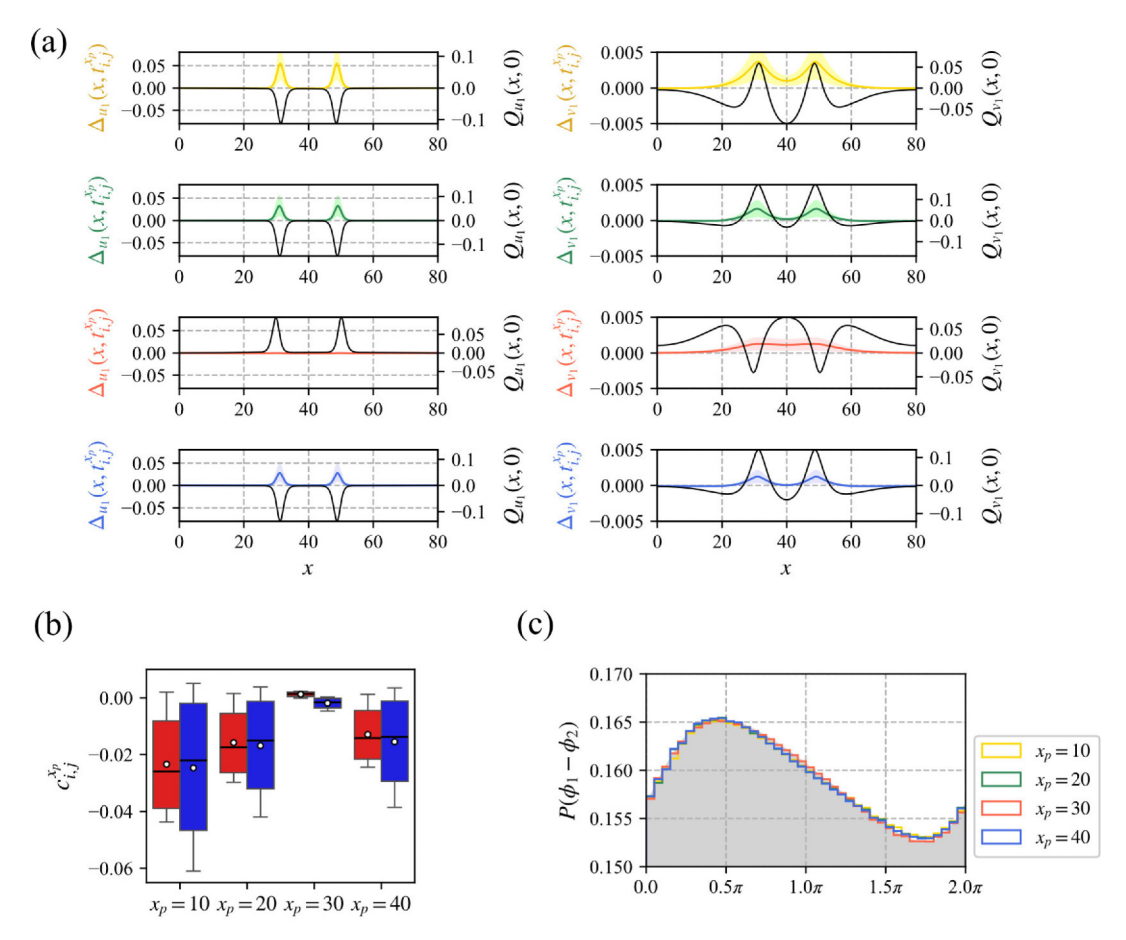


FIG. 14. Calculation of the correction terms and the phase for the spatiotemporal dynamics exhibiting oscillating spots from measurements taken at a single spatial grid point (Appendix G). (a) Distribution of $\Delta_{u_1}(x, t_{1,j}^{x_p})$ and $\Delta_{v_1}(x, t_{1,j}^{x_p})$ under the condition of $x_p = 10$ (first row), 20 (second row), 30 (third row), and 40 (fourth row), along with the phase sensitivity functions, $Q_{u_1}(x, 0)$ and $Q_{v_1}(x, 0)$. The left figures display $\Delta_{u_1}(x, t_{1,j}^{x_p})$ and $Q_{u_1}(x, 0)$, and the right figures display $\Delta_{v_1}(x, t_{1,j})$ and $Q_{v_1}(x, 0)$. The colored lines indicate the medians of $\Delta_{u_1}(x, t_{1,j}^{x_p})$ and $\Delta_{v_1}(x, t_{1,j}^{x_p})$. The colored shades indicate the range between the 25th and 75th percentiles. The black lines indicate $Q_{u_1}(x, 0)$ and $Q_{v_1}(x, 0)$. (b) Statistics of the correction term $c_{i,j}^{x_p}$ for each x_p . The red (i = 1) and blue (i = 2) boxes represent the first and third quartiles of dataset $\{c_{i,j}^{x_p}\}_j$. The horizontal lines mark the medians, while the dots mark the averages. The whiskers extend to show the maximum and minimum values. (c) Histograms of $\phi_1 - \phi_2$ for $x_p = 10$ (yellow), 20 (green), 30 (red), and 40 (blue). The histograms are calculated over a duration in which $|\phi_1 - \phi_2|$ increases by 200π . The distribution calculated from the phase equations is displayed in gray.

consider $X_{i,n_p}^{k_p}(t_{i,j}^{k_p}) - \chi_{i,n_p}^{k_p}(0) = 0$, we obtain Eq. (11). From this derivation, it follows that $Q_{i,n}^k(0)$ in Eq. (11) represents the linear response characteristics of the phase to deviations of $X_{i,n}^k$ from the state of $\phi_i = 0$ on the limit-cycle solution.

APPENDIX G: PHASE CALCULATION FOR OSCILLATING SPOTS

In this appendix, we investigate phase calculation for spatiotemporal dynamics exhibiting oscillating spots, applying the same methods used for target waves (Secs. IV and V). The first subsection describes the FHN reaction-diffusion model for numerical simulation. The second to fourth subsections describe the application of each phase calculation method.

1. Numerical simulation

To generate spatiotemporal dynamics with oscillating spots, we conducted a numerical simulation using the FHN

reaction-diffusion model [Eqs. (1) and (2)]. The spacedependent parameter $\alpha(x) = \alpha_0 + (\alpha_1 - \alpha_0)(2x/L - 1)^2$ is the largest at the center (x = L/2) and smallest at the boundaries (x = 0, L). The other parameters are $a_0 = -1.1$, $a_1 = 1.6$, $\gamma = 2.0$, $\tau_1^{-1} = 0.03$, $\tau_2^{-1} = 0.028$, $\kappa_1 = 1.0$, $\kappa_2 = 0.9$, $\delta_1 = 2.5$, and $\delta_2 = 2.4$. The periods of the limitcycle solutions are $T_1 \simeq 195.3$ and $T_2 \simeq 212.2$. The coupling intensity is $K = \text{diag}(1.0 \times 10^{-4}, 0)$. For the numerical simulation, we used a one-dimensional system of size L=80with no-flux boundary conditions. The system is discretized into spatial grids with $\Delta x = L/2^8$. Time integration starts $u_1(x, 0) = v_1(x, 0) = -0.424 + \sin[1.133 + (x/L)\pi]$ $u_2(x, 0) = v_2(x, 0) = -0.993 + \sin[0.122 + (x/L)\pi].$ The initial time evolution up to 5.0×10^4 is discarded, and measurements are taken from the subsequent evolution over a duration of 3.0×10^5 . Time integration was performed using the explicit Heun scheme with a time step $\Delta t = 0.01$.

Under these conditions, oscillating spots constrained at the center are generated. Figure 12(a) shows the spatiotemporal

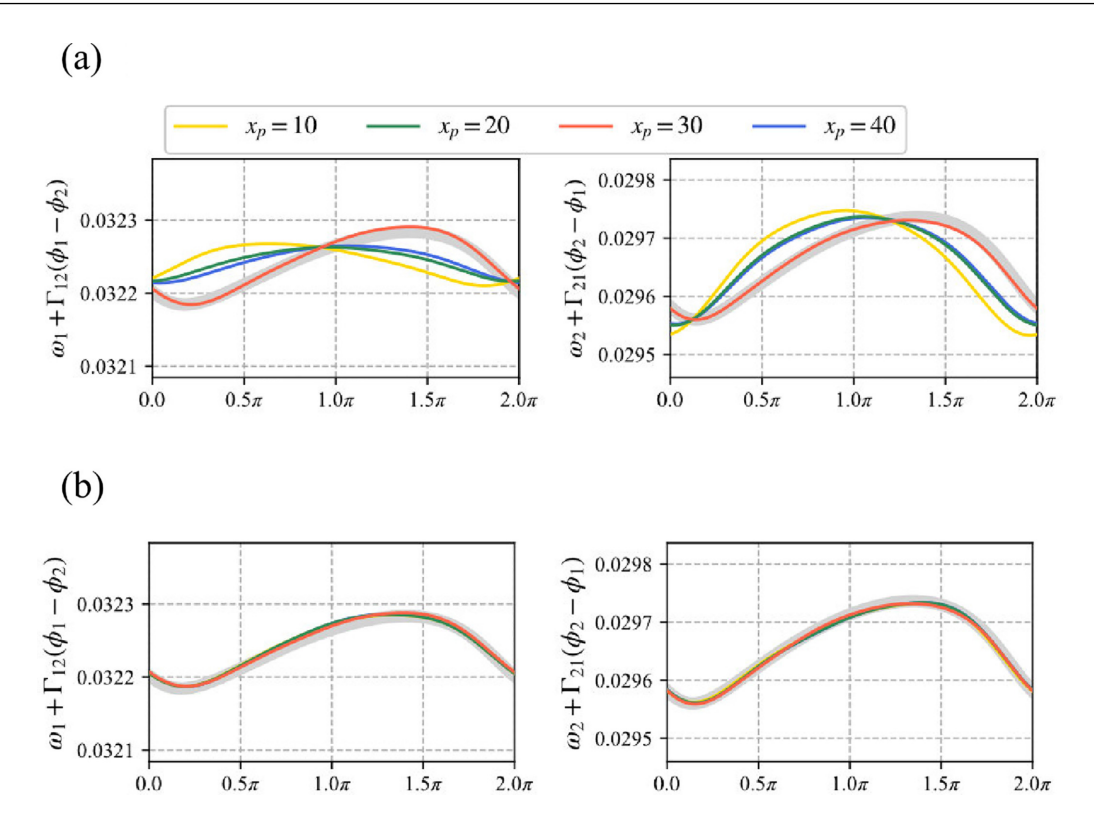


FIG. 15. Similar to Fig. 9, but these results are obtained from measurements of spatiotemporal dynamics exhibiting oscillating spots (Appendix G) instead of target waves. (a) Results obtained from $\theta_i^{x_p}$. (b) Results obtained from ϕ_i .

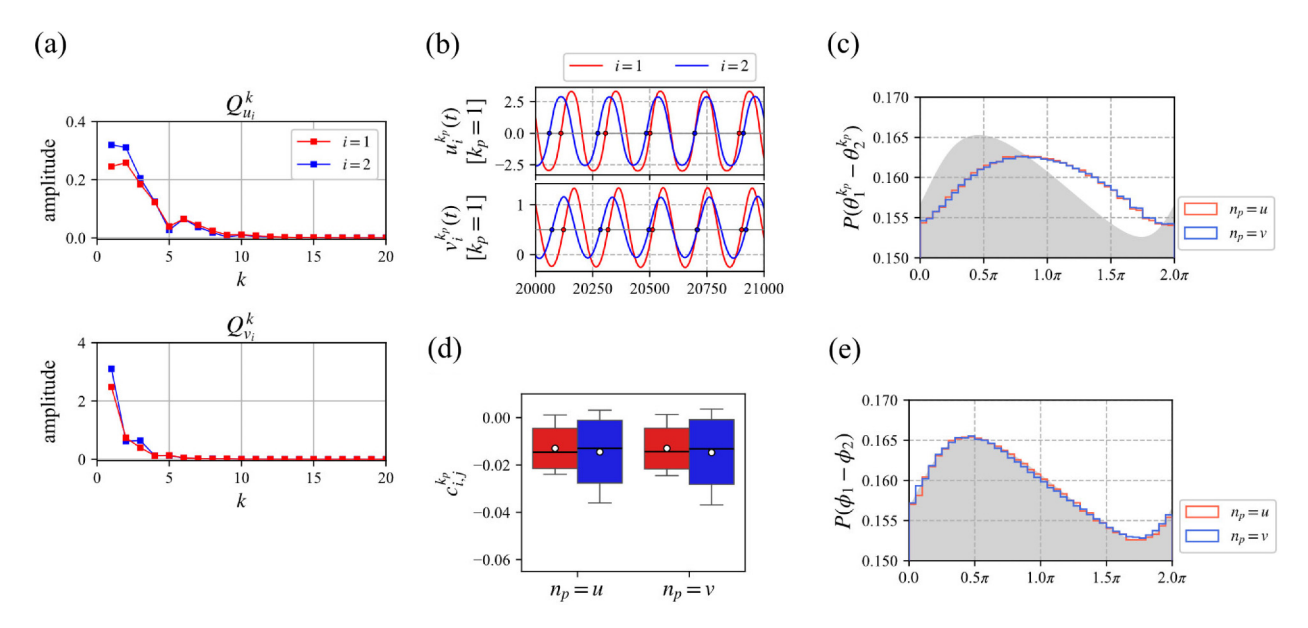


FIG. 16. Calculation of the phase of spatiotemporal dynamics exhibiting oscillating spots from measurements on all spatial grid points (Appendix G). The decomposition scheme described in Sec. V D is used, and $k_p=1$ is adopted. (a) Amplitude of $Q_{u_i}^k$ (top) and $Q_{v_i}^k$ (bottom). The amplitude of $Q_{u_i}^k$ is calculated by $\int_0^{2\pi} |Q_{u_i}^k(\psi)| d\psi/2\pi$ (a similar formula is used for $Q_{v_i}^k$). The red and blue lines indicate i=1 and i=2, respectively. (b) Time series of $u_i^{k_p}(t)$ (top) and $v_i^{k_p}(t)$ (bottom) and the Poincaré sections. The red and blue lines indicate i=1 and i=2, respectively. The horizontal lines represent the Poincaré sections, and the dots represent the times when $u_i^{k_p}(t)$ or $v_i^{k_p}(t)$ intersects the Poincaré section from negative to positive. (c) Histograms of $\theta_1^{k_p} - \theta_2^{k_p}$ for $n_p = u$ (red) and $n_p = v$ (blue). The histograms are calculated over a duration in which $|\theta_1^{k_p} - \theta_2^{k_p}|$ increases by 200π . The distribution calculated from the phase equations is displayed in gray. (d) Statistics of the correction term $c_{i,j}^{k_p}$ for both $n_p = u$ and $n_p = v$. The red (i=1) and blue (i=2) boxes represent the first and third quartiles of dataset $\{c_{i,j}^{k_p}\}_j$. The horizontal lines mark the medians, while the dots mark the averages. The whiskers extend to show the maximum and minimum values. (e) Histograms of $\phi_1 - \phi_2$ for $n_p = u$ (red) and $n_p = v$ (blue). The histograms are calculated over a duration in which $|\phi_1 - \phi_2|$ increases by 200π . The distribution calculated from the phase equations is displayed in gray.

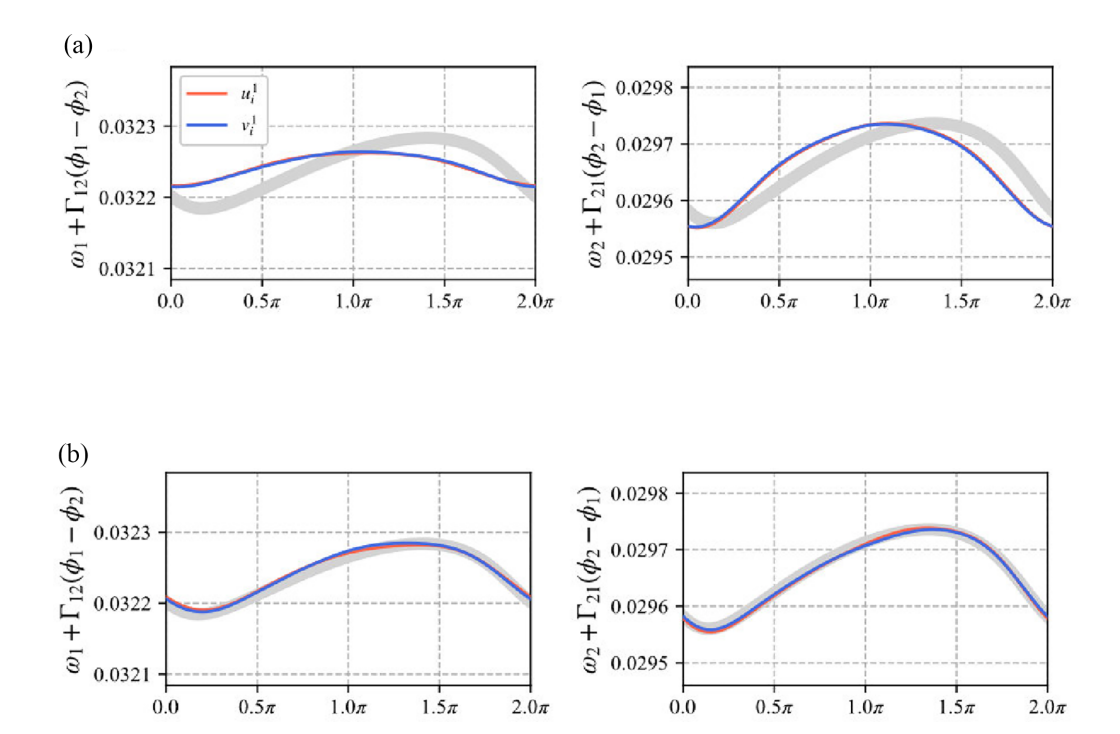


FIG. 17. Similar to Fig. 10, but these results are obtained from measurements of spatiotemporal dynamics exhibiting oscillating spots (Appendix G) instead of target waves. (a) Results obtained from $\theta_i^{x_p}$. (b) Results obtained from ϕ_i .

dynamics of u_1 and v_1 . The oscillating spot, characterized by large values of u_i and v_i , can be seen rhythmically expanding and contracting. The fronts of the oscillating spot for u_i appear sharply. Therefore, the time series of $u_i(x_p, t)$ measured in the region where the spot's fronts oscillate shows intermittent sharp increases and decreases. In contrast, in other regions, the time series of $u_i(x_p, t)$ exhibits only slight variations without abrupt changes. The limit-cycle solution and the phase sensitivity function are shown in Figs. 12(b) and 12(c), respectively. The phase sensitivity function is localized at the spot's front. This fact indicates that the region where the front exists influences the rhythm of the entire system.

2. Calculating the phase from a measurement on a single spatial grid point

We focus on the phase calculation that relies on measurements from a single spatial grid point. We implement the approach described in Sec. IV for oscillating spots. The time series of $\theta_i^{x_p}(t)$ was calculated from that of $u_i(x_p,t)$ for $x_p=10,20,30,40$. Only $x_p=30$ is located in the region containing the spot's front, where the phase sensitivity function is localized. Examples of the time series of $u_i(x_p,t)$ and the Poincaré sections for each x_p are shown in Fig. 13(a). According to Fig. 13(b), the difference between the histogram of $\theta_1^{x_p}-\theta_2^{x_p}$ and the distribution of $\phi_1-\phi_2$ calculated from the phase equation is the smallest for $x_p=30$. Therefore, the approach described in Sec. IV B is effective for oscillating spots.

Figure 14(a) shows the distribution of $\Delta_{u_i}(x, t_{i,j}^{x_p})$ and $\Delta_{v_i}(x, t_{i,j}^{x_p})$ as well as $Q_{u_i}(x, 0)$ and $Q_{v_i}(x, 0)$. The figure indicates that the region with large $|\Delta_{u_i}(x, t_{i,j}^{x_p})|$ do not overlap

the region with large $|Q_{u_i}(x, 0)|$ only for $x_p = 30$ (the same is true for Q_{v_i} and Δ_{v_i}). Given this result, the magnitude of the correction term is notably small only for $x_p = 30$. The statistics of the correction term indicate that the correction term is close to zero for $x_p = 30$ [Fig. 14(b)].

As with the target waves (Sec. IV C), ignoring the correction term changes the phase calculation results, and the extent of this change depends on the correction term. Figure 14(c) shows the histograms of $\phi_1 - \phi_2$ calculated on the basis of Eqs. (5) and (6). The histograms of $\phi_1 - \phi_2$ for each x_p are almost similar, although the histogram of $\theta_1^{x_p} - \theta_2^{x_p}$ shown in Fig. 13(b) varies depending on x_p . It is evident that the histograms of $\theta_1^{x_p} - \theta_2^{x_p}$ and $\phi_1 - \phi_2$ differ significantly for $x_p = 10, 20, 40$ since the magnitude of the correction term is large, but they are similar for $x_p = 30$ since the correction term is nearly zero. Ignoring the correction term degrades the accuracy of phase equation estimation unless the correction term is nearly zero. Figures 15(a) and 15(b) show the phase equations estimated from the time series of $\theta_i^{\lambda_p}(t)$ and $\phi_i(t)$, respectively. The phase equations estimated from $\theta_i^{x_p}$ differ significantly from the true forms for $x_p = 10, 20, 40,$ but closely match the true forms for $x_p = 30$. In contrast, the phase equations estimated from ϕ_i are consistent with the true forms regardless of x_p .

3. Calculating the phase from measurements on all spatial grid points

We shift focus to methods involving measurements from all spatial grid points. We implement the decomposition scheme described in Sec. VD for spatiotemporal dynamics exhibiting oscillating spots as we do for target waves. Since the ampli-

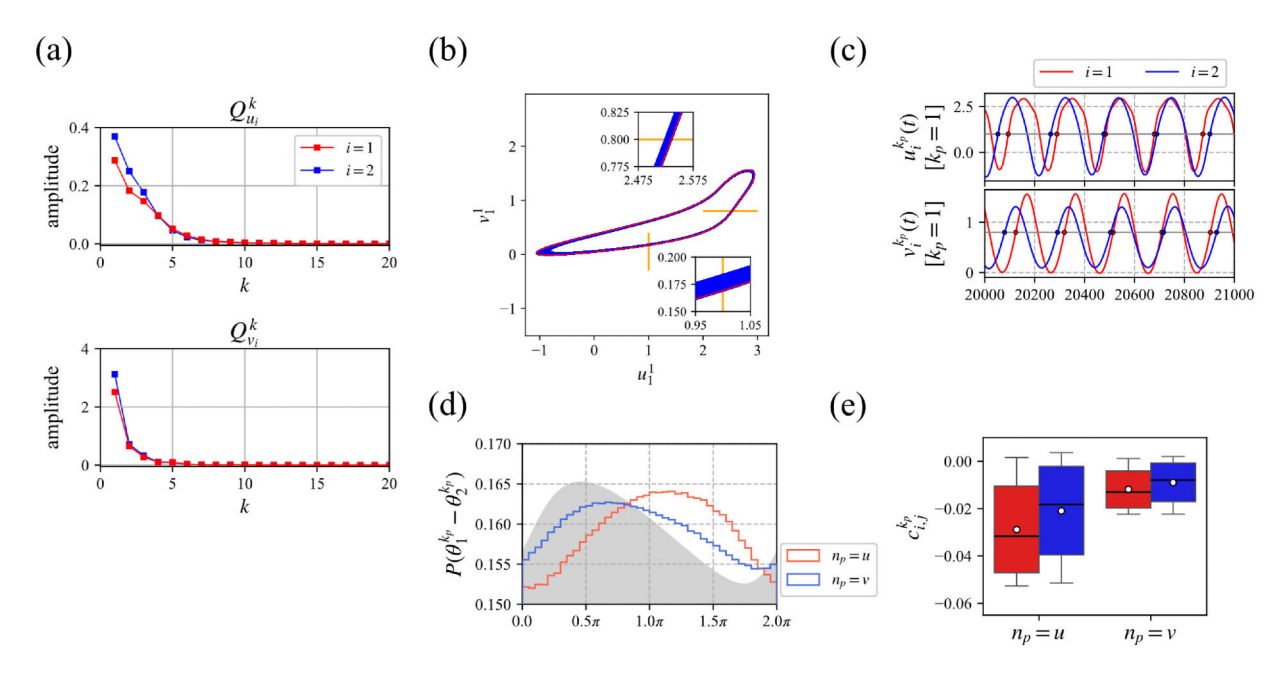


FIG. 18. Calculation of the phase of spatiotemporal dynamics exhibiting oscillating spots from measurements on all spatial grid points (Appendix G). The decomposition scheme described in Sec. V E is used, and $k_p=1$ is adopted. (a) Amplitude of $Q_{u_i}^k$ (top) and $Q_{v_i}^k$ (bottom). The amplitude of $Q_{u_i}^k$ is calculated by $\int_0^{2\pi} |Q_{u_i}^k(\psi)| \mathrm{d}\psi/2\pi$ (a similar formula is used for $Q_{v_i}^k$). The red and blue lines indicate i=1 and i=2, respectively. The amplitudes are not localized to a small number of $Q_{u_i}^k$ and $Q_{v_i}^k$ despite the implementation of the scheme described in Sec. V E. (b) Trajectory of (u_1^1, v_1^1) (blue) and the limit-cycle of $(\chi_{u_1}^1, \chi_{v_1}^1)$ (red). The Poincaré sections for $n_p=u$ and $n_p=v$ are depicted with yellow lines, and the insets provide a close-up view around the intersection. (c) Time series of $u_i^{k_p}(t)$ (top) and $v_i^{k_p}(t)$ (bottom) and the Poincaré sections. The red and blue lines represent i=1 and i=2, respectively. The horizontal lines represent the Poincaré sections, and the dots represent the times when $u_i^{k_p}(t)$ or $v_i^{k_p}(t)$ intersects the Poincaré section from negative to positive. (d) Histograms of $\theta_1^{k_p}-\theta_2^{k_p}$ for $n_p=u$ (red) and $n_p=v$ (blue). The histograms are calculated over a duration in which $|\theta_1^{k_p}-\theta_2^{k_p}|$ increases by 200π . The distribution calculated from the phase equations is displayed in gray. (e) Statistics of the correction term $c_{i,j}^{k_p}$ for both $n_p=u$ and $n_p=v$. The red (i=1) and blue (i=2) boxes represent the first and third quartiles of dataset $\{c_{i,j}^{k_p}\}_j$. The horizontal lines mark the medians, while the dots mark the averages. The whiskers extend to show the maximum and minimum values.

tude of $Q_{u_i}^k$ and $Q_{v_i}^k$ up to about k=5 are nonzero [Fig. 16(a)], the fluctuations in the corresponding u_i^k and v_i^k influence the correction term. We applied the Poincaré section to either time series of $u_i^{k_p}$ or $v_i^{k_p}$ ($k_p=1$) to calculate $\theta_i^{k_p}$ as shown in Fig. 16(b). The histograms of $\theta_1^{k_p}(t)-\theta_2^{k_p}$ shown in Fig. 16(c) differs from the distribution of $\phi_1-\phi_2$ calculated from the phase equations. The large difference between the histogram and distribution is supported by the statistics of the correction term shown in Fig. 16(d). The statistics indicate that the magnitude of the correction term is comparable to those calculated

from $u_i(x_p, t)$ for $x_p = 10$, 20, 40 [Fig. 14(b)]. Figure 16(e) indicates that both histograms of $\phi_1 - \phi_2$, which are calculated from the time series of isochron-based phases, are similar to the distribution calculated from the phase equations. These findings validate that the correction term represents the difference between $\theta_i^{k_p}(t_{i,j}^{k_p})$ and $\phi_i(t_{i,j}^{k_p})$. Furthermore, Figs. 17(a) and 17(b) show the phase equations estimated from the time series of $\theta_i^{k_p}$ and ϕ_i , respectively. The phase equations estimated from $\theta_i^{k_p}$ deviate from the true forms while those estimated from ϕ_i closely match the true forms.

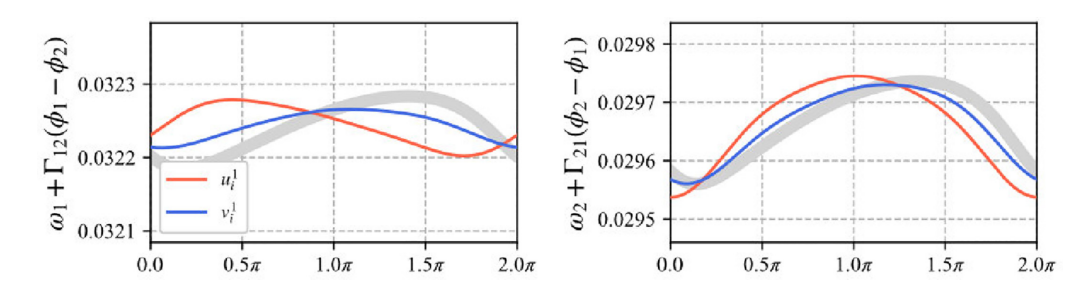


FIG. 19. Similar to Fig. 11, but these results are obtained from measurements of spatiotemporal dynamics exhibiting oscillating spots (Appendix G) instead of target waves.

4. Case of using the basis function obtained from the phase sensitivity function

We also implement another scheme of orthogonal decomposition implemented in Sec. V E. Figure 18(a) indicates that $Q_{u_i}^k$ and $Q_{v_i}^k$ up to about k=5 have nonzero amplitude. Therefore, fluctuations in u_i^k and v_i^k up to about k=5 determine the correction terms. Figure 18(b) shows the deviation of the trajectory of (u_1^1, v_1^1) from the limit-cycle of $(\chi_{u_1}^1, \chi_{v_i}^1)$ is larger compared to the target waves shown in Fig. 7(b). Thus, the magnitude of the correction term is likely to be larger for oscillating spots than for target waves. We applied the

Poincaré section to the time series of $u_i^{k_p}$ or $v_i^{k_p}$ ($k_p=1$) to calculate $\theta_i^{k_p}$ [Fig. 18(c)]. The histograms of $\theta_1^{k_p} - \theta_2^{k_p}$ differ from the distribution of $\phi_1 - \phi_2$ calculated from the phase equations [Fig. 18(d)]. Furthermore, the statistics of the correction term shown in Fig. 18(e) indicate that its magnitude is comparable to that shown in Fig. 16(d). These results indicate that this PCA-based scheme does not reduce the magnitude of the correction term. Furthermore, ignoring the correction term degrades the accuracy of the phase equation estimation. Figure 19 shows that the phase equations estimated from the time series of $\theta_i^{k_p}$ differ from the true forms.

- A. T. Winfree, The Geometry of Biological Time (Springer, New York, 1980).
- [2] Y. Kuramoto, Chemical Oscillations, Waves, and Turbulence (Springer, New York, 1984).
- [3] E. Brown, J. Moehlis, and P. Holmes, On the phase reduction and response dynamics of neural oscillator populations, Neural Comput. **16**, 673 (2004).
- [4] B. Ermentrout, Type I membranes, phase resetting curves, and synchrony, Neural Comput. **8**, 979 (1996).
- [5] B. Ermentrout and D. H. Terman, Mathematical Foundations of Neuroscience (Springer, New York, 2010).
- [6] F. C. Hoppensteadt, E. M. Ižikevič, and E. M. Izhikevich, Weakly Connected Neural Networks (Springer, New York, 1997).
- [7] E. M. Izhikevich, Dynamical Systems in Neuroscience: The Geometry of Excitability and Bursting (MIT Press, Cambridge, MA, 2006).
- [8] M. G. Rosenblum and A. S. Pikovsky, Detecting direction of coupling in interacting oscillators, Phys. Rev. E 64, 045202(R) (2001)
- [9] R. F. Galan, G. B. Ermentrout, and N. N. Urban, Efficient estimation of phase-resetting curves in real neurons and its significance for neural-network modeling, Phys. Rev. Lett. 94, 158101 (2005).
- [10] G. B. Ermentrout, R. F. Galan, and N. N. Urban, Relating neural dynamics to neural coding, Phys. Rev. Lett. 99, 248103 (2007).
- [11] K. Ota, M. Nomura, and T. Aoyagi, Weighted spike-triggered average of a fluctuating stimulus yielding the phase response curve, Phys. Rev. Lett. 103, 024101 (2009).
- [12] T. Imai, K. Ota, and T. Aoyagi, Robust measurements of phase response curves realized via multicycle weighted spiketriggered averages, J. Phys. Soc. Jpn. 86, 024009 (2017).
- [13] R. Cestnik and M. Rosenblum, Reconstructing networks of pulse-coupled oscillators from spike trains, Phys. Rev. E 96, 012209 (2017).
- [14] R. Cestnik and M. Rosenblum, Inferring the phase response curve from observation of a continuously perturbed oscillator, Sci. Rep. 8, 13606 (2018).
- [15] J. Miyazaki and S. Kinoshita, Determination of a coupling function in multicoupled oscillators, Phys. Rev. Lett. 96, 194101 (2006).
- [16] I. T. Tokuda, S. Jain, I. Z. Kiss, and J. L. Hudson, Inferring phase equations from multivariate time series, Phys. Rev. Lett. 99, 064101 (2007).

- [17] B. Kralemann, L. Cimponeriu, M. Rosenblum, A. Pikovsky, and R. Mrowka, Uncovering interaction of coupled oscillators from data, Phys. Rev. E **76**, 055201(R) (2007).
- [18] B. Kralemann, L. Cimponeriu, M. Rosenblum, A. Pikovsky, and R. Mrowka, Phase dynamics of coupled oscillators reconstructed from data, Phys. Rev. E 77, 066205 (2008).
- [19] T. Stankovski, A. Duggento, P. V. E. McClintock, and A. Stefanovska, Inference of time-evolving coupled dynamical systems in the presence of noise, Phys. Rev. Lett. 109, 024101 (2012).
- [20] A. Duggento, T. Stankovski, P. V. E. McClintock, and A. Stefanovska, Dynamical Bayesian inference of time-evolving interactions: From a pair of coupled oscillators to networks of oscillators, Phys. Rev. E 86, 061126 (2012).
- [21] B. Kralemann, M. Frühwirth, A. Pikovsky, M. Rosenblum, T. Kenner, J. Schaefer, and M. Moser, *In vivo* cardiac phase response curve elucidates human respiratory heart rate variability, Nat. Commun. 4, 2418 (2013).
- [22] K. Ota and T. Aoyagi, Direct extraction of phase dynamics from fluctuating rhythmic data based on a Bayesian approach, arXiv:1405.4126.
- [23] T. Stankovski, T. Pereira, P. V. E. McClintock, and A. Stefanovska, Coupling functions: Universal insights into dynamical interaction mechanisms, Rev. Mod. Phys. 89, 045001 (2017).
- [24] A. Matsuki, H. Kori, and R. Kobayashi, Network inference from oscillatory signals based on circle map, arXiv:2407.07445.
- [25] S. Revzen and J. M. Guckenheimer, Estimating the phase of synchronized oscillators, Phys. Rev. E 78, 051907 (2008).
- [26] M. Rosenblum, A. Pikovsky, A. A. Kühn, and J. L. Busch, Real-time estimation of phase and amplitude with application to neural data, Sci. Rep. 11, 18037 (2021).
- [27] S. Wilshin, M. D. Kvalheim, C. Scott, and S. Revzen, Estimating phase from observed trajectories using the temporal 1-form, arXiv:2203.04498.
- [28] E. Gengel and A. Pikovsky, Phase reconstruction from oscillatory data with iterated Hilbert transform embeddings—Benefits and limitations, Physica D 429, 133070 (2022).
- [29] A. Matsuki, H. Kori, and R. Kobayashi, An extended Hilbert transform method for reconstructing the phase from an oscillatory signal, Sci. Rep. 13, 3535 (2023).
- [30] N. Namura, S. Takata, K. Yamaguchi, R. Kobayashi, and H. Nakao, Estimating asymptotic phase and amplitude functions of

- limit-cycle oscillators from time series data, Phys. Rev. E **106**, 014204 (2022).
- [31] Y. Hashimoto, M. Ikeda, H. Nakao, and Y. Kawahara, Datadriven operator-theoretic analysis of weak interactions in synchronized network dynamics, arXiv:2208.06186.
- [32] S. Shirasaka, W. Kurebayashi, and H. Nakao, Phase-amplitude reduction of transient dynamics far from attractors for limitcycling systems, Chaos 27, 023119 (2017).
- [33] A. Mauroy and I. Mezić, Global computation of phaseamplitude reduction for limit-cycle dynamics, Chaos 28, 073108 (2018).
- [34] K. Fukami, H. Nakao, and K. Taira, Data-driven transient lift attenuation for extreme vortex gust-airfoil interactions, J. Fluid Mech. 992, A17 (2024).
- [35] K. Yawata, K. Fukami, K. Taira, and H. Nakao, Phase autoencoder for limit-cycle oscillators, Chaos 34, 063111 (2024).
- [36] T. Stankovski, Time-varying coupling functions: Dynamical inference and cause of synchronization transitions, Phys. Rev. E 95, 022206 (2017).
- [37] T. Stankovski, V. Ticcinelli, P. V. E. McClintock, and A. Stefanovska, Neural cross-frequency coupling functions, Front. Syst. Neurosci. 11, 33 (2017).
- [38] T. Onojima, T. Goto, H. Mizuhara, and T. Aoyagi, A dynamical systems approach for estimating phase interactions between rhythms of different frequencies from experimental data, PLoS Comput. Biol. 14, e1005928 (2018).
- [39] K. Suzuki, T. Aoyagi, and K. Kitano, Bayesian estimation of phase dynamics based on partially sampled spikes generated by realistic model neurons, Front. Comput. Neurosci. 11, 116 (2018).
- [40] K. Ota, I. Aihara, and T. Aoyagi, Interaction mechanisms quantified from dynamical features of frog choruses, R. Soc. Open Sci. 7, 191693 (2020).
- [41] T. Arai, Y. Kawamura, and T. Aoyagi, Extracting phase coupling functions between collectively oscillating networks from time-series data, J. Phys. Soc. Jpn. **91**, 124001 (2022).
- [42] T. Arai, K. Ota, T. Funato, K. Tsuchiya, T. Aoyagi, and S. Aoi, Interlimb coordination is not strictly controlled during walking, Commun. Biol. 7, 1152 (2024).
- [43] H. Furukawa, T. Arai, T. Funato, S. Aoi, and T. Aoyagi, Bayesian estimation of trunk-leg coordination during walking using phase oscillator models, bioRxiv:2024.04.25.591041 [Neurosci. Research (to be published)].
- [44] K. Stein, A. Timmermann, and N. Schneider, Phase synchronization of the El Niño-Southern oscillation with the annual cycle, Phys. Rev. Lett. 107, 128501 (2011).
- [45] K. Stein, A. Timmermann, N. Schneider, F.-F. Jin, and M. F. Stuecker, ENSO seasonal synchronization theory, J. Clim. 27, 5285 (2014).
- [46] T. Kohyama, Y. Yamagami, H. Miura, S. Kido, H. Tatebe, and M. Watanabe, The gulf stream and Kuroshio current are synchronized, Science 374, 341 (2021).
- [47] P. Cessi, Gulf Stream and Kuroshio synchronization, Science 374, 259 (2021).
- [48] Y. Tachibana, Y. Inoue, K. K. Komatsu, T. Nakamura, M. Honda, K. Ogata, and K. Yamazaki, Interhemispheric synchronization between the AO and the AAO, Geophys. Res. Lett. 45, 13,477 (2018).
- [49] H. Kori, Y. Kawamura, H. Nakao, K. Arai, and Y. Kuramoto, Collective-phase description of coupled oscillators

- with general network structure, Phys. Rev. E **80**, 036207 (2009).
- [50] Y. Kawamura, H. Nakao, and Y. Kuramoto, Collective phase description of globally coupled excitable elements, Phys. Rev. E **84**, 046211 (2011).
- [51] Y. Kawamura, Collective phase reduction of globally coupled noisy dynamical elements, Phys. Rev. E 95, 032225 (2017).
- [52] H. Nakao, S. Yasui, M. Ota, K. Arai, and Y. Kawamura, Phase reduction and synchronization of a network of coupled dynamical elements exhibiting collective oscillations, Chaos 28, 045103 (2018).
- [53] Y. Kawamura and H. Nakao, Collective phase description of oscillatory convection, Chaos 23, 043129 (2013).
- [54] Y. Kawamura and H. Nakao, Noise-induced synchronization of oscillatory convection and its optimization, Phys. Rev. E 89, 012912 (2014).
- [55] Y. Kawamura and H. Nakao, Phase description of oscillatory convection with a spatially translational mode, Physica D 295-296, 11 (2015).
- [56] H. Nakao, T. Yanagita, and Y. Kawamura, Phase-reduction approach to synchronization of spatiotemporal rhythms in reaction-diffusion systems, Phys. Rev. X 4, 021032 (2014).
- [57] Y. Kawamura, S. Shirasaka, T. Yanagita, and H. Nakao, Optimizing mutual synchronization of rhythmic spatiotemporal patterns in reaction-diffusion systems, Phys. Rev. E 96, 012224 (2017).
- [58] K. Taira and H. Nakao, Phase-response analysis of synchronization for periodic flows, J. Fluid Mech. 846, R2 (2018).
- [59] M. Iima, Jacobian-free algorithm to calculate the phase sensitivity function in the phase reduction theory and its applications to Kármán's vortex street, Phys. Rev. E **99**, 062203 (2019).
- [60] M. Iima, Phase reduction technique on a target region, Phys. Rev. E 103, 053303 (2021).
- [61] Y. Kawamura, V. Godavarthi, and K. Taira, Adjoint-based phase reduction analysis of incompressible periodic flows, Phys. Rev. Fluids 7, 104401 (2022).
- [62] V. Godavarthi, Y. Kawamura, and K. Taira, Optimal waveform for fast synchronization of airfoil wakes, J. Fluid Mech. 976, R1 (2023).
- [63] M. Iima, Optimal external forces of the lock-in phenomena for flow past an inclined plate in uniform flow, Phys. Rev. E 109, 045102 (2024).
- [64] Y. Kawamura and R. Tsubaki, Phase reduction approach to elastohydrodynamic synchronization of beating flagella, Phys. Rev. E 97, 022212 (2018).
- [65] J. Löber and H. Engel, Controlling the position of traveling waves in reaction-diffusion systems, Phys. Rev. Lett. 112, 148305 (2014).
- [66] J. Löber, M. Bär, and H. Engel, Front propagation in onedimensional spatially periodic bistable media, Phys. Rev. E 86, 066210 (2012).
- [67] G. B. Ermentrout, J. Z. Jalics, and J. E. Rubin, Stimulus-driven traveling solutions in continuum neuronal models with a general smooth firing rate function, SIAM J. Appl. Math. 70, 3039 (2010).
- [68] T. Ohta, Pulse dynamics in a reaction–diffusion system, Physica D 151, 61 (2001).
- [69] H. Mori and Y. Kuramoto, *Dissipative Structures and Chaos* (Springer, Berlin, 1997).

- [70] M. C. Cross and P. C. Hohenberg, Pattern formation outside of equilibrium, Rev. Mod. Phys. 65, 851 (1993).
- [71] S.-I. Ei, The motion of weakly interacting pulses in reaction-diffusion systems, J. Dyn. Diff. Equ. 14, 85 (2002).
- [72] P. Manneville, Dissipative Structures and Weak Turbulence, Perspectives in Physics (Academic Press, San Diego, 1990).
- [73] J. J. Tyson and J. P. Keener, Singular perturbation theory of traveling waves in excitable media (a review), Physica D 32, 327 (1988).
- [74] K. Taira, S. L. Brunton, S. T. M. Dawson, C. W. Rowley, T. Colonius, B. J. McKeon, O. T. Schmidt, S. Gordeyev, V. Theofilis, and L. S. Ukeiley, Modal analysis of fluid flows: An overview, AIAA J. 55, 4013 (2017).
- [75] S. P. Hastings, On the existence of homoclinic and periodic orbits for the FitzHugh-Nagumo equations, Q. J. Math. 27, 123 (1976).
- [76] A. Hagberg and E. Meron, Pattern formation in non-gradient reaction-diffusion systems: The effects of front bifurcations, Nonlinearity 7, 805 (1994).
- [77] T. Nomura and L. Glass, Entrainment and termination of reentrant wave propagation in a periodically stimulated ring of excitable media, Phys. Rev. E 53, 6353 (1996).
- [78] T. Yanagita, H. Suetani, and K. Aihara, Bifurcation analysis of solitary and synchronized pulses and formation of reentrant waves in laterally coupled excitable fibers, Phys. Rev. E 78, 056208 (2008).
- [79] Y. Kawamura, Phase synchronization between collective rhythms of fully locked oscillator groups, Sci. Rep. 4, 4832 (2015).

- [80] P. L. Read and A. A. Castrejón-Pita, Phase synchronization between stratospheric and tropospheric quasi-biennial and semi-annual oscillations, Q. J. R. Meteorol. Soc. 138, 1338 (2012).
- [81] K. Rajendran, I. M. Moroz, P. L. Read, and S. M. Osprey, Synchronisation of the equatorial QBO by the annual cycle in tropical upwelling in a warming climate, Q. J. R. Meteorol. Soc. 142, 1111 (2016).
- [82] I. Z. Kiss, Y. Zhai, and J. L. Hudson, Emerging coherence in a population of chemical oscillators, Science 296, 1676 (2002).
- [83] T. Nakagaki, H. Yamada, and T. Ueda, Interaction between cell shape and contraction pattern in the Physarum plasmodium, Biophys. Chem. **84**, 195 (2000).
- [84] M. R. Guevara, L. Glass, and A. Shrier, Phase locking, period-doubling bifurcations, and irregular dynamics in periodically stimulated cardiac cells, Science 214, 1350 (1981).
- [85] M. Hildebrand, J. Cui, E. Mihaliuk, J. Wang, and K. Showalter, Synchronization of spatiotemporal patterns in locally coupled excitable media, Phys. Rev. E 68, 026205 (2003).
- [86] M. O. Williams, I. G. Kevrekidis, and C. W. Rowley, A data-driven approximation of the Koopman operator: Extending dynamic mode decomposition, J. Nonlinear Sci. 25, 1307 (2015).
- [87] M. Korda and I. Mezić, On convergence of extended dynamic mode decomposition to the Koopman operator, J. Nonlinear Sci. 28, 687 (2018).
- [88] Y. Kawamura, Phase reduction of limit-torus solutions to partial differential algebraic equations, Phys. Rev. Res. 1, 033130 (2019).